Structural and Multidisciplinary Optimization (2026) 69:107
https://doi.org/10.1007/s00158-026-04319-5

RESEARCH PAPER

Automated adaptive resolution framework with self-adjusting barrier regularization for stable nonlinear isogeometric topology optimization

Xinqing Li[1,2] · Zhen-Pei Wang[2] · Yongzhen Mi[2] · David W. Rosen[2,3] · Yingjun Wang[1]

Received: 29 September 2025 / Revised: 4 February 2026 / Accepted: 21 March 2026 / Published online: 9 April 2026
© The Author(s), under exclusive licence to Springer-Verlag GmbH Germany, part of Springer Nature 2026

Abstract
The iterative process of nonlinear analysis in topology optimization leads to high computational cost. To improve efficiency and convergence, a common strategy is to use a finer mesh for design and a coarser mesh for analysis. Coarse analysis meshes offer three key advantages: (1) faster convergence, (2) reduced computational time per iteration, and (3) lower risk of mesh distortion. However, the resolution mismatch can result in non-physical discontinuous material distributions within analysis elements, exhibiting characteristics of numerical artifacts of material discontinuities (i.e., QR-patterns). Multiresolution schemes, which decouple the design and analysis discretizations, can alleviate the above issues. To fully exploit the advantages of multiresolution schemes, we propose an *h*-refinement-based automated adaptive resolution method within the framework of isogeometric analysis. In this approach, an objective-based QR-patterns detection algorithm is activated during the convergence phase of the optimization. If QR-patterns are identified, the analysis mesh is automatically refined, thereby achieving an improved balance between accuracy and efficiency. Moreover, we propose a self-adjusting barrier regularization method that is particularly effective for large deformations and multiresolution meshes. This method automatically imposes penalties to resist mesh distortion, and further improving computational efficiency. Numerical results demonstrate that, compared to fixed-resolution strategies, the proposed adaptive framework achieves a superior trade-off between accuracy and cost. An additional contribution is a manufacturing-friendly post-processing strategy based on NURBS representation, enabling direct export of editable CAD models. Several numerical examples highlight the method's advantages in terms of computational efficiency, geometric fidelity, and stability under large-deformation conditions.

Keywords Adaptive resolution · Self-adjusting barrier regularization · Nonlinear · Isogeometric topology optimization · Post-processing

1 Introduction

1.1 Nonlinear topology optimization: necessity, computational burden, and mesh distortion

Topology optimization (TO) is a powerful structural design method that determines the optimal material distribution within a given design domain to maximize system

Responsible Editor: Xiaojia Shelly Zhang.

Yongzhen Mi
mi_yongzhen@a-star.edu.sg

Yingjun Wang
wangyj84@scut.edu.cn

1 National Engineering Research Center of Novel Equipment for Polymer Processing, The Key Laboratory of Polymer Processing Engineering of the Ministry of Education, Guangdong Provincial Key Laboratory of Technique and Equipment for Macromolecular Advanced Manufacturing, South China University of Technology, Guangzhou 510641, China

2 Institute of High Performance Computing (IHPC), Agency for Science, Technology and Research (A*STAR), 1 Fusionopolis Way, #16-16 Connexis, Singapore 138632, Singapore

3 Agency for Science, Technology and Research (A*STAR), Singapore Institute of Manufacturing Technology (SIMTech), 5 Cleantech Loop #01-01, Singapore 636732, Singapore

performance under specific constraints. While traditional TO has achieved significant success in linear elastic regimes under small-deformation assumptions, modern high-performance structures often exhibit geometric and material nonlinearity (Bodaghi et al. 2024), especially in emerging applications like 4D-printed soft systems (Zolfagharian et al. 2020; Tian et al. 2022) that undergo large deformations. In such contexts, traditional linear elastic topology optimization can produce designs that perform poorly or even fail when subjected to real nonlinear behavior. Incorporating nonlinear finite deformation mechanics (e.g., finite-strain hyperelastic material models (Han et al. 2024, 2025)) into topology optimization is therefore essential to accurately capture phenomena like dramatic shape changes, stress stiffening or softening, and material yielding. Early pioneering works extended topology optimization to geometrically nonlinear regimes, demonstrating that considering large-deformation effects yields more reliable compliant mechanism designs and robust structures. For instance, Buhl et al. (2000) included incremental geometric nonlinearity in stiffness design, and Bruns and Tortorelli (2001) introduced a framework for nonlinear elastic materials. These studies confirmed that nonlinear topology optimization (TO) can produce fundamentally different (and more accurate) optimal layouts compared to linear formulations, particularly for applications requiring extensive flexibility or soft material response.

However, the inclusion of nonlinear analysis drastically increases the computational burden (Yin et al. 2025). Each design iteration entails solving a nonlinear finite element analysis (FEA), typically requiring iterative Newton–Raphson equilibrium solves and possibly multiple load increments for convergence. This is far more time-consuming than a single linear solve per iteration. Consequently, scalability emerges as a major challenge: high-resolution designs with nonlinear FEA can be prohibitively expensive. Researchers have proposed various strategies to mitigate this cost. Some approaches reduce the number of design variables or use coarse surrogate models (Behrou et al. 2021; Li et al. 2022), while others develop specialized solvers and continuation schemes for the nonlinear state equation (Träff et al. 2023; Gomes and Senne 2014). Nonetheless, fully resolving fine-scale topology details under nonlinear physics remains computationally intensive.

Another difficulty in nonlinear TO is maintaining solution stability and accuracy in the presence of large deformations. As the structure deforms significantly, the finite element mesh can suffer severe mesh distortion (element skewing or even inversion), especially in regions that become nearly void or extremely thin. This distortion can cause numerical ill-conditioning or failure in the analysis (Scherz et al. 2024). Methods to cope with this include adaptive re-meshing (Schillinger et al. 2012), element deletion (Bruns and Tortorelli 2003), or adding stabilization terms (Bluhm et al. 2021; Frederiksen et al. 2025). For example, van Dijk et al. (2014) introduced an element deformation scaling technique to improve robustness of geometrically nonlinear analysis in TO. Likewise, Lahuerta et al. (2013) proposed stabilization schemes for low-density elements under large strain. Wang et al. (2014) proposed an energy interpolation method to prevent excessive deformation caused by insufficient stiffness in low-density regions. These techniques seek to prevent the unintended collapse of nearly empty elements that could otherwise lead to singular stiffness matrices or non-convergent simulations. Even with such measures, achieving convergence in nonlinear TO can be delicate, often requiring careful load stepping and damping, which further contributes to the computational cost. Recently, we (Li et al. 2025a, b) proposed a Jacobian-based barrier regularization method that, from a geometric perspective, regulates the Jacobian of element mappings to improve mesh quality, offering a new approach to address mesh distortion under large deformations.

In recent years, isogeometric analysis (IGA) has emerged as a valuable tool to address some of these challenges in TO. IGA uses smooth spline-based basis functions (e.g., NURBS) for FEA, unifying the CAD geometry and analysis model (Hughes et al 2005; Cottrell et al. 2009). Building on this integration of design and analysis, researchers have explored extensions of IGA to shape optimization (Wang et al. 2017) and, more importantly, to topology optimization, which has led to the development of isogeometric topology optimization (ITO) (Wang et al. 2018; Gao et al. 2020). Since its inception, ITO has evolved rapidly. Early foundational works established the framework using trimmed surfaces (Seo et al. 2010) and density fields in B-spline space (Qian 2013). More recently, the scope of ITO has been significantly broadened to handle complex engineering challenges, such as multipatch cellular structures using Nitsche's method (Gao et al. 2023), aerodynamic optimization of thin shells via T-splines (Zhang et al. 2025), and particle flow problems using the isogeometric material point method (Lin et al. 2025). Specifically for nonlinear TO, IGA offers distinct advantages: smooth basis functions better capture large deformations, and simple h-refinement facilitates multiresolution frameworks. Consequently, recent studies have begun to extend ITO to geometrically nonlinear regimes. For instance, Jahangiry et al. (2022) combined level sets with IGA for nonlinear plane stress problem, and Liu et al. (2025) investigated geometrically nonlinear ITO to improve structural performance under large deformation. While these works demonstrate that IGA improves analysis fidelity, it does not alone solve the issue of computational expense at high resolution. This motivates the use of multiresolution strategies, discussed next, which in combination with IGA and nonlinear analysis can significantly alleviate the computational burden.

1.2 Multiresolution strategies: benefits and limitations

A promising strategy to reduce the cost of nonlinear topology optimization is multiresolution discretization, where a fine mesh is used for the design variables and a coarse mesh for finite element analysis (FEA). Originally proposed by Nguyen et al. (2010; 2012), this decoupling allows each coarse element to contain multiple fine design voxels, enabling high-resolution topology descriptions without solving a large FEA system. By doing so, one can attain high resolution, intricate designs without the need to solve an extremely large FEA system at every iteration. Currently, this method has been extensively applied to address complex topology optimization problems, including multimaterial (Park et al. 2021), uncertainty (Keshavarzzadeh et al. 2019), and multiscale (Xu et al. 2019) scenarios.

Beyond linear problems, the benefits of multiresolution discretization become even more pronounced in nonlinear topology optimization. The coarse analysis mesh dramatically saves the computational costs stemming from three primary reasons: First, a coarser analysis mesh leads to a lower-dimensional tangent stiffness matrix, which corresponds to the Hessian matrix in Newton–Raphson-based nonlinear solvers. As a result, the analysis converges more rapidly, often requiring fewer iterations per load step. Second, the coarse mesh involves fewer degrees of freedom (DoFs), thereby reducing the computational time needed for solving the equilibrium equations in each analysis step. Together, these factors substantially decrease the per-iteration time cost compared to fine-mesh nonlinear analysis. Thirdly, a coarse analysis mesh enhances robustness against distortion by avoiding small, easily inverted elements, allowing stable nonlinear analysis even under large deformations. Ortigosa and Martínez-Frutos (2021) proposed a novel multiresolution topology optimization framework for nonlinear electroactive shell structures, featuring: (1) an in-plane adaptive resolution scheme enabling higher-density discretization on material surfaces and (2) numerical determination of critical density-resolution-to-filter-length ratios to suppress QR-patterns in nonlinear electromechanical systems, revealing more flexible bounds than linear elasticity cases. Chen et al. (2022) proposed a multiresolution nonlinear topology optimization method based on the multiresolution design strategy and additive hyperelasticity technique to address the computational burden and convergence difficulties in nonlinear topology optimization involving geometric and material nonlinearity.

In addition, multiresolution strategies have also been introduced into isogeometric topology optimization. The combination is particularly appealing, since the smooth and CAD-exact NURBS basis functions not only facilitate the mapping between fine design fields and coarse analysis meshes, but also enhance robustness against mesh distortion while ensuring high geometric fidelity. Lieu et al. (2017a) proposed a multiresolution topology optimization framework based on isogeometric analysis, in which design variables are defined in an auxiliary parameter space and mapped to the analysis domain using bivariate B-spline basis functions. This approach enables efficient multiresolution optimization while leveraging the geometric exactness and high continuity of NURBS in IGA. They further extended this framework to multimaterial topology optimization (Lieu and Lee 2017b). Du et al. (2020) proposed an explicit ITO method based on moving morphable voids, incorporating a novel multiresolution scheme with separate discretization levels for geometry and analysis. However, existing multiresolution ITO approaches are based on *k*-refinement, which constructs nested meshes by increasing the polynomial order of the basis functions without altering the degree of freedom distribution. While this approach maintains continuity and compatibility, it has limited capability in capturing localized structural details and struggles to balance computational efficiency with expressive design resolution.

Despite these advantages, the mismatch between the fine design field and coarse analysis can produce QR-patterns, artificial stiffness artifacts caused by disconnected high-density regions within coarse elements (Gupta et al. 2018). These patterns lead to stiffness overestimation due to the inability of low-order shape functions to capture discontinuous deformation, risking invalid or misleading designs. To suppress them, large-density filters are commonly applied to enforce smooth intra-element density, but this blurs fine features and degrades design quality. Attempts to reduce filter size for sharper topology often reintroduce QR-patterns, revealing a trade-off between resolution and robustness. Gupta et al. (2018) systematically analyzed this issue and provided filter guidelines based on shape function order, but filter-based remedies inevitably sacrifice design fidelity. This motivates the need for localized, automated solutions, such as adaptive analysis refinement, to preserve both accuracy and efficiency.

1.3 Adaptive resolution framework with self-adjusting barrier regularization

To address the limitations of fixed multiresolution schemes and large-deformation mesh distortion, we propose an automated adaptive resolution isogeometric topology optimization framework with self-adjusting barrier regularization method. The key idea is to apply adaptive *h*-refinement to the IGA analysis mesh, triggered by a compliance-based QR-pattern detection algorithm to automatically choose different analysis meshes to ensure a good balance between design accuracy and analysis efficiency. Moreover, to ensure a stable optimization process, a self-adjusting barrier regularization term is also introduced to penalize severe mesh distortion in nonlinear analysis by embedding a Jacobian-dependent energy term that diverges as elements approach unacceptable levels of distortion. Finally, we introduce a CAD-compatible post-processing step that extracts smooth boundaries, yielding ready-to-print models with geometric continuity.

The remainder of this paper is organized as follows: Sect. 2 provides the problem statement, covering isogeometric analysis and nonlinear topology optimization. Section 3 describes the adaptive resolution framework with self-adjusting barrier regularization and the overall optimization procedure with the post-processing. Section 4 evaluates the performance of the multiresolution analysis and optimization procedures through benchmark examples. Section 5 demonstrates the applicability and generality of the proposed method using representative structural design problems. Section 6 concludes the paper and discusses future research directions.

2 Problem statement

2.1 Isogeometric concept

Non-uniform rational B-splines (NURBS) are geometric modeling tools that combine flexibility and accuracy, widely used in computer-aided design (CAD) and numerical analysis (Li et al. 2025a, b). Compared to traditional polynomial basis functions, NURBS can not only precisely reproduce freeform curves and surfaces but also accurately represent analytic geometries such as circular arcs and ellipses. As such, they serve as ideal representations for both geometry and field variables in IGA. The key advantage of NURBS lies in the introduction of weight parameters w, which embed rational functions into the B-spline framework, enabling a unified representation of a wide variety of engineering geometries. This enhances the geometric accuracy and computational robustness in numerical simulations.

The construction of B-splines is based on the definition of knot vectors and basis functions. A knot vector is an ordered, non-decreasing sequence of parameter values, typically denoted as $\Xi = \left\{\xi_0, \xi_1, \cdots, \xi_{n+p}\right\}$, where n is the number of control points and p is the spline degree. Based on the given knot vector, B-spline basis functions are generated using the Cox-de Boor recursive formula (Piegl and Tiller 1995).

$$
\begin{aligned}
N_{i,0}(\xi) &= \begin{cases} 1 & if\ \xi_i \le \xi < \xi_{i+1} \\ 0 & Otherwise \end{cases} \\
N_{i,p}(\xi) &= \frac{(\xi-\xi_i)N_{i,p-1}(\xi)}{\xi_{i+p}-\xi_i} + \frac{(\xi_{i+p+1}-\xi)N_{i+1,p-1}(\xi)}{\xi_{i+p+1}-\xi_{i+1}} \quad if\ \ \xi_i \le \xi < \xi_{i+1}
\end{aligned}
\tag{1}
$$

Specifically, the zeroth-order basis functions ($p=0$) are piecewise constant functions. Higher-order basis functions are constructed via linear interpolation and recursive combination, ensuring local support and higher-order continuity. This recursive definition grants NURBS excellent smoothness and controllability, making them suitable for high-precision geometric modeling and analysis of complex engineering structures (Li et al. 2024).

NURBS basis functions are defined by rationalizing B-spline functions as follows:

$$
R_{i,p}(\xi) = \frac{N_{i,p}(\xi)w_i}{\sum_j^n N_{j,p}(\xi)w_j}, \tag{2}
$$

According to the property of tensor products, the two-dimensional NURBS basis functions are constructed as:

$$
R_{i,j}(\xi,\eta) = \frac{N_{i,p}(\xi)N_{j,q}(\eta)w_{i,j}}{\sum_{k=0}^n N_{k,p}(\xi)N_{k,q}(\eta)w_{k,l}}, \tag{3}
$$

2.2 Neo-Hookean hyperelastic model

To accurately describe the nonlinear material behavior of structures under large-deformation conditions, this study adopts the compressible Neo-Hookean hyperelastic model (Klarbring and Strömberg 2013). The strain energy density function for the Neo-Hookean model is defined as:

$$
W = \frac{\mu}{2}(\mathrm{tr}(\boldsymbol{C}) - 3) - \mu \ln J + \frac{\lambda}{2}(\ln J)^2, \tag{4}
$$

where μ and λ are Lamé constants, controlling the shear modulus and bulk modulus, $\boldsymbol{C} = \boldsymbol{F}^{\mathrm{T}}\boldsymbol{F}$ is the right Cauchy-Green tensor, where $\boldsymbol{F}$ is the deformation gradient, which describes the mapping of material points from the reference configuration to the current configuration and is defined as:

$$
\boldsymbol{F} = \boldsymbol{I} + \frac{\partial \boldsymbol{u}}{\partial \boldsymbol{X}}, \tag{5}
$$

where $\boldsymbol{X}$ is the initial position vector and $\boldsymbol{I}$ is the identity matrix, and J is the Jacobian determinant, defined as $J = \det(\boldsymbol{F})$. The relationship between the Lamé parameters and the macroscopic material properties (Young's modulus E_0 and Poisson's ratio ν) is:

$$\mu = \frac{E_0}{2(1+\nu)}, \lambda = \frac{\nu E_0}{(1+\nu)(1-2\nu)}, \tag{6}$$

2.3 Nonlinear isogeometric analysis

In large-deformation analysis, the Jacobian determinant may fluctuate significantly within elements, leading to the accumulation of numerical integration errors and the singularity of the stiffness matrix. To mitigate this issue, this study incorporates the Jacobian barrier regularization term into the total potential energy functional, constructing a novel energy expression to improve numerical stability and computational robustness in large-deformation hyperelastic problems. The modified potential energy form is:

$$\tilde{\Pi}(\boldsymbol{u}) = \Pi(\boldsymbol{u}) + \int_{\Omega_0} \psi(J(\boldsymbol{u}))dV, \tag{7}$$

where ψ represents the barrier regularization term, and $\boldsymbol{u}$ is the displacement vector.

The second-order variation of this modified potential energy functional leads to the tangent stiffness matrix:

$$\boldsymbol{K} = \frac{\partial^2 \tilde{\Pi}}{\partial \boldsymbol{u}^2} = \boldsymbol{K}_{\text{mat}} + \boldsymbol{K}_{\text{geo}} + \boldsymbol{K}_{\text{bar}}, \tag{8}$$

where $\boldsymbol{K}_{\text{mat}}$ and $\boldsymbol{K}_{\text{geo}}$ represent the material and geometric stiffness matrices, respectively, defined as:

$$\boldsymbol{K}_{\text{mat}} = \int_{\Omega} \boldsymbol{B}^{\text{T}}\boldsymbol{D}\boldsymbol{B}dV, \quad \boldsymbol{K}_{\text{geo}} = \int_{\Omega} \boldsymbol{G}^{\text{T}}\boldsymbol{S}\boldsymbol{G}dV, \tag{9}$$

where, $\boldsymbol{B}$ is constructed from the deformation gradient-related term matrix $\boldsymbol{F}_G$ and the shape function derivative matrix $\boldsymbol{G}$. For two-dimensional problems, they are defined as:

$$\boldsymbol{B} = \boldsymbol{F}_G\boldsymbol{G} = \begin{bmatrix} \frac{\partial u}{\partial X}+1 & \frac{\partial v}{\partial X} & 0 & 0 \\ 0 & 0 & \frac{\partial u}{\partial Y} & \frac{\partial v}{\partial Y}+1 \\ \frac{\partial u}{\partial Y} & \frac{\partial v}{\partial Y}+1 & \frac{\partial u}{\partial X}+1 & \frac{\partial v}{\partial X} \end{bmatrix} \begin{bmatrix} \frac{\partial N_1}{\partial X} & 0 & \frac{\partial N_2}{\partial X} & 0 & \dots & \frac{\partial N_n}{\partial X} & 0 \\ 0 & \frac{\partial N_1}{\partial X} & 0 & \frac{\partial N_2}{\partial X} & \dots & 0 & \frac{\partial N_n}{\partial X} \\ \frac{\partial N_1}{\partial Y} & 0 & \frac{\partial N_2}{\partial Y} & 0 & \dots & \frac{\partial N_n}{\partial Y} & 0 \\ 0 & \frac{\partial N_1}{\partial Y} & 0 & \frac{\partial N_2}{\partial Y} & \dots & 0 & \frac{\partial N_n}{\partial Y} \end{bmatrix}, \tag{10}$$

where (u, v) represent the displacement fields in the 2D problem, (X, Y) are the initial coordinates, and $n = 9$ represents the number of control points in an element.

The barrier stiffness matrix $\boldsymbol{K}_{\text{bar}}$, derived from the second-order variation of the barrier regularization term, is:

$$\boldsymbol{K}_{\text{bar}} = \frac{\partial^2 \psi(J)}{\partial \boldsymbol{u}^2} = \int_{\Omega} \frac{\partial^2 \psi}{\partial J^2}\boldsymbol{B}^{\text{T}}\boldsymbol{B}dV, \tag{11}$$

This modified potential energy form introduces the geometric mapping distortion penalty term directly at the energy functional level. Without introducing additional numerical parameters or artificial criteria, it achieves good locality and geometric consistency, making it particularly suitable for topology optimization problems in isogeometric high-order continuous frameworks.

To solve the large-deformation equilibrium equations, this study uses the Newton-Simpson iterative method for incremental updates. At each iteration step k, the displacement increment is updated by solving the following linearized equation:

$$\boldsymbol{K}^{(k)}\Delta\boldsymbol{u}^{(k)} = \boldsymbol{R}^{(k)}, \tag{12}$$

where $\boldsymbol{R}$ is the residual force vector, defined as:

$$\boldsymbol{R} = \boldsymbol{f}_{\text{ext}} - \boldsymbol{f}_{\text{int}}, \tag{13}$$

where $\boldsymbol{f}_{\text{int}}$ represents the internal force vector under the current configuration, and $\boldsymbol{f}_{\text{ext}}$ is the external load vector. The equilibrium state corresponds to $\boldsymbol{R} = \boldsymbol{0}$.

In each iteration, the displacement field is updated incrementally by accumulating the displacement changes.

$$\boldsymbol{u}^{(k+1)} = \boldsymbol{u}^{(k)} + \Delta\boldsymbol{u}^{(k)}, \tag{14}$$

And the convergence is assessed based on the relative L_2-norm of the displacement increments between two consecutive steps:

$$e_{\text{tol}} = \frac{\|\Delta\boldsymbol{u}\|_2}{\|\boldsymbol{u}\|_2}, \tag{15}$$

where e_{tol} represents the convergence tolerance.

2.4 Nonlinear topology optimization

In conventional nonlinear topology optimization, $E_{\min}$ is often used to assign a very small stiffness to void regions to prevent numerical singularities caused by zero-stiffness elements during nonlinear analysis (Sigmund 2007). Unlike the modified SIMP method, this work does not introduce a minimum modulus parameter $E_{\min}$. This is because the self-adjusting barrier regularization provides a natural stabilization mechanism. The total stiffness matrix is the sum of the density-dependent stiffness terms

($\boldsymbol{K}_{\text{mat}}+\boldsymbol{K}_{\text{geo}}$) and the density-independent barrier stiffness ($\boldsymbol{K}_{\text{bar}}$). In void regions, while the material and geometric stiffness vanishes, the barrier term, derived strictly from the barrier regularization term, effectively acts as a numerical background stiffness. This term ensures that the global stiffness matrix remains positive definite and non-singular, maintaining numerical stability even in the complete absence of physical material.

This work adopts the standard Solid Isotropic Material with Penalization (SIMP) material interpolation scheme to link design variables to material stiffness. The interpolation relationship is defined as:

$$E(x) = \rho_e^{\alpha} E_0, \tag{16}$$

where $\rho_e \in [0, 1]$ is the design variable (element density), α is the penalty factor, and E_0 is the Young's modulus of the base material.

We introduce the topology optimization problem under material and geometric nonlinearity. Two optimization objectives are considered, (i) Minimum compliance design: maximizing the overall structural stiffness, (ii) Compliant mechanism design: maximizing the displacement at a specific output point. Both problems are formulated under a nonlinear IGA framework and can be unified as follows:

$$\begin{aligned} &\min_{0\le\rho_e\le 1}\ :\ \ C(\boldsymbol{\rho}) = \boldsymbol{L}^{\mathrm{T}}\boldsymbol{u} \\ &\quad \text{s.t.:}\ \ \boldsymbol{R}(\boldsymbol{\rho},\boldsymbol{u}) = \boldsymbol{0} \\ &g = \sum_{e=1}^{n_e} \rho_e v_e - V \le 0 \end{aligned} \tag{17}$$

where $\boldsymbol{L}$ is the generalized load vector: for compliance minimization, $\boldsymbol{L}=\boldsymbol{f}_{\text{ext}}$, and for compliant mechanism design, $\boldsymbol{L}$ is 1 at the output degree of freedom and 0 elsewhere. The constraint function g limits the total material volume, where n_e is the total number of elements, v_e is the volume of element e, and V is the prescribed volume.

The sensitivity of the objective function can be derived using the Lagrange multiplier method:

$$\frac{\partial C}{\partial \rho_e} = \boldsymbol{L}(\xi,\eta)\frac{\partial \boldsymbol{u}}{\partial \rho_e} + \boldsymbol{\vartheta}^{\mathrm{T}}\left(\frac{\partial \boldsymbol{R}}{\partial \rho_e} + \frac{\partial \boldsymbol{R}}{\partial \boldsymbol{u}}\frac{\partial \boldsymbol{u}}{\partial \rho_e}\right), \tag{18}$$

Combining the SIMP interpolation and the adjoint method, the sensitivity expression becomes:

$$\frac{\partial C}{\partial \rho_e} = -\boldsymbol{\vartheta}^{\mathrm{T}}(\alpha\rho_e^{\alpha-1}E_0)\boldsymbol{f}_{\text{int}}(\xi,\eta), \tag{19}$$

where the adjoint variable $\boldsymbol{\vartheta}$ is determined by solving the adjoint equation:

$$\boldsymbol{K}\boldsymbol{\vartheta} = \boldsymbol{L}, \tag{20}$$

To prevent numerical instabilities such as checkerboard patterns and zigzag boundaries (Sigmund 1997), a sensitivity filter (Sigmund 1994) is used to process the sensitivities of the objective function. The filtered sensitivity expression is given by:

$$\widehat{\frac{\partial C}{\partial \rho_e}} = \frac{1}{\max(\varsigma,\rho_e)\sum_{i\in N_e} H_{ei}} \sum_{i\in N_e} H_{ei}\rho_e\frac{\partial C}{\partial \rho_e}, \tag{21}$$

where ς is a small positive constant to prevent division by zero, N_e is the set of elements within the filter radius, and H_{ei} is the filter weight.

In addition, the Optimality Criteria (OC) method is adopted to solve the topology optimization problem.

3 Adaptive multiresolution framework with self-adjusting barrier regularization for stable optimization

3.1 H-refinement multiresolution isogeometric framework

In SIMP-based topology optimization, the finite element analysis mesh and the material density mesh are typically fully coupled. To achieve a refined topological structure, it is often necessary to refine the analysis mesh accordingly, which significantly increases the degrees of freedom and computational cost.

To improve computational efficiency in nonlinear topology optimization while ensuring high-resolution optimized results, we propose a multiresolution ITO framework based on h-refinement. This approach integrates the concept of multiresolution topology optimization with nonlinear IGA techniques. By performing nonlinear analysis on a coarse mesh and describing the topology design on a fine mesh, it effectively decouples the design domain from the analysis domain, significantly reducing computational cost and enhancing design flexibility, as illustrated in Fig. 1.

The proposed multiresolution framework consists of two types of discretized mesh domains: the analysis mesh domain, and the design density mesh domain. The analysis domain employs a coarse mesh for nonlinear IGA, along with the corresponding NURBS integration points and basis functions. The design domain uses a fine density mesh for the subsequent optimization process, incorporating the refined NURBS integration points and basis functions after h-refinement.

Figure 2 illustrates the multiresolution design and analysis meshes used in our isogeometric topology

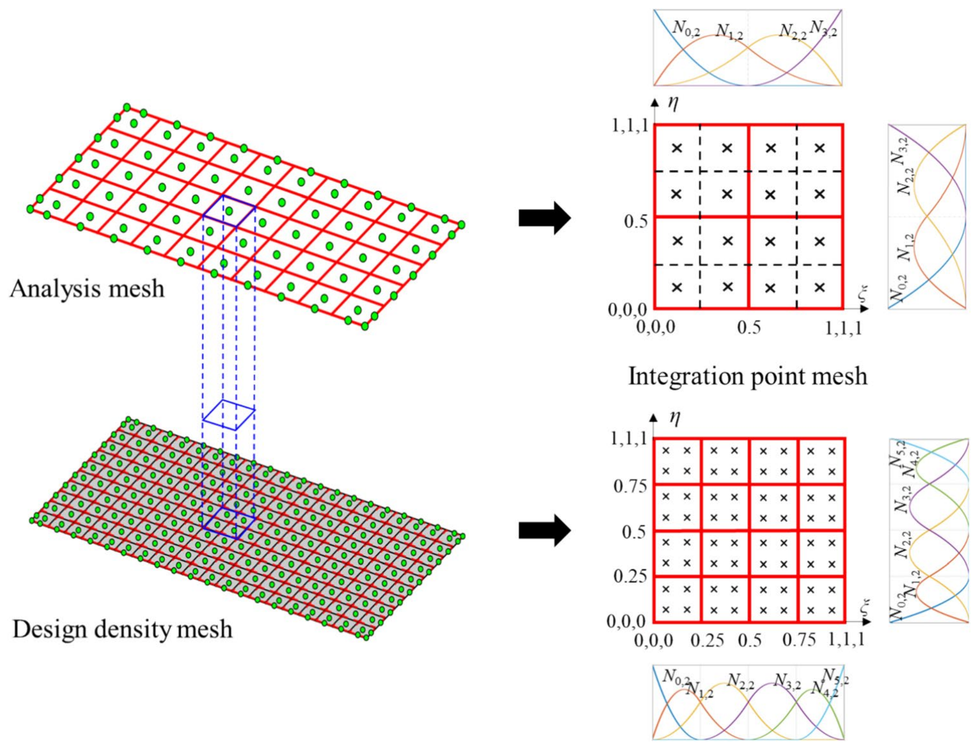

Fig. 1 Structure diagram of multiresolution IGA, analysis mesh + integration point mesh, design density mesh + integration point mesh

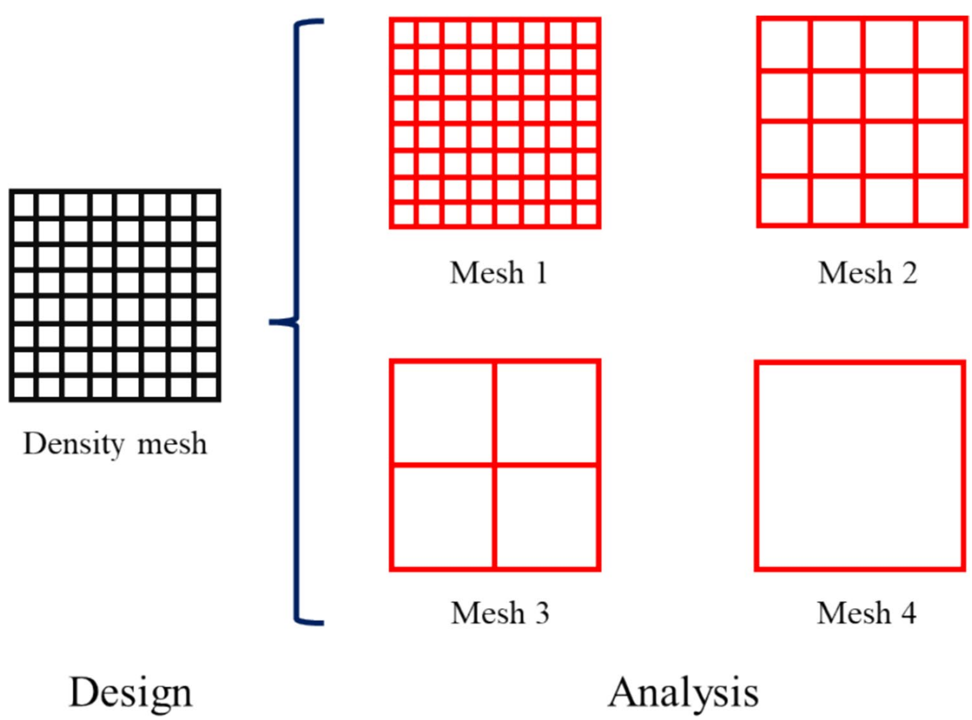

Fig. 2 The design and analysis meshes of multiresolution framework

optimization framework. The figure on the left (in black) represents the high-resolution design density mesh, which captures detailed optimization configuration with fine discretization. The red meshes on the right illustrate the four types of analysis meshes employed in this study.

Given a 2D problem with a design density mesh of $N_x \times N_y$, corresponding to $N_x \times N_y$ design variables, where N_x and N_y represent the number of elements in the x and y directions, respectively. The DoF of the same analysis

Table 1 DoFs for three design density meshes with $p = q = 2$

Density mesh number	Mesh 1	Mesh 2	Mesh 3	Mesh 4	Max. ratio
8×8	200	72	32	18	11.11
40×40	3,528	968	288	98	36
400×400	323,208	81,608	20,808	5408	59.76

The maximum ratio here refers to the DoF ratio between Mesh 1 and Mesh 4

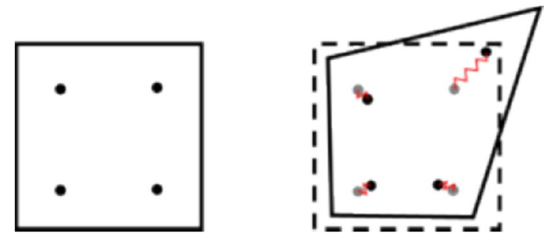

Fig. 3 Schematic diagram for suppressing grid distortion

mesh (Mesh 1) is $(N_x + p) \times (N_x + q) \times 2$ where $(N_x + p)$ and $(N_x + q)$ are the number of control points along the two directions, respectively. For Meshes 2, 3, and 4, the DoFs are $(N_x/2 + p) \times (N_x/2 + q) \times 2$, $(N_x/4 + p) \times (N_x/4 + q) \times 2$, and $(N_x/8 + p) \times (N_x/8 + q) \times 2$, respectively. The DoFs for three different design density meshes with degrees of 2 in both directions are given in Table 1, where it shows that when using a design density mesh of 400×400, the DoF ratio of Mesh 1 and Mesh 4 can reach to 59.76, indicating a significant demand of computational resource.

3.2 Self-adjusting barrier regularization method

In large-deformation nonlinear analysis, the Jacobian determinant approaching zero or even becoming negative can lead to numerical integration errors, ill-conditioned matrices, failure in solver convergence, and mesh distortion. For the previous barrier regularization method, the penalty coefficient usually needs to be prescribed manually, but its selection inevitably affects the analysis results. This study proposes a self-adjusting barrier regularization method in which the barrier coefficient automatically adjusts according to the degree of mesh distortion, thereby avoiding the uncertainty associated with manually prescribed parameters and repeated trial-and-error tuning.

First, the barrier threshold δ (typically chosen as $0 < \delta \ll 1$) must be specified. When the Jacobian determinant falls below δ, it is set to $J = \delta$. The self-adjusting barrier (SA-barrier) term is defined as:

$$\psi(J) = -\gamma \log(J) = -\gamma \log(\det(\boldsymbol{F})), \tag{22}$$

where γ is the barrier coefficient, which is self-adjusted according to the variation in the Jacobian determinant within each element, defined as:

$$\gamma = 0.001 + 0.01\left(J_{\max} - J_{\min}\right), \tag{23}$$

where the baseline barrier coefficient 0.001 is set to a constant value. This selection follows the empirical strategy established in our previous work (Li et al. 2025b). The value is chosen to be sufficiently small to ensure that the barrier energy contributes negligibly to the total potential energy in well-behaved mesh regions thereby preserving physical accuracy. Conversely, combined with the dynamic scaling term $0.01(J_{\max}—J_{\min})$, it provides adequate penalty forces to effectively suppress mesh distortion when the Jacobian determinant approaches the critical threshold or becomes negative. $J_{\max}$ and $J_{\min}$ are the maximum and minimum values of $\det(\boldsymbol{F})$ among all Gauss points within the current element, respectively.

For numerical implementation, to ensure consistency and efficiency with the energy functional, the stiffness contribution (Hessian approximation) is obtained by taking the second derivative of ψ

$$\phi(J) = \frac{\partial^2 \psi}{\partial J^2} = \frac{0.001 + 0.01(J_{\max} - J_{\min})}{J^2}, \tag{24}$$

Furthermore, the barrier stiffness matrix $\boldsymbol{K}_{\text{bar}}$ can be obtained,

$$\boldsymbol{K}_{\text{bar}} = \int_{\Omega} \phi(J) \boldsymbol{B}^{\mathrm{T}} \boldsymbol{B} dV, \tag{25}$$

From a mechanical perspective, although the self-adjusting barrier method is primarily introduced to enhance numerical stability, it embodies a geometric motivated energy regularization mechanism. Specifically, the barrier term increases asymptotically as the Jacobian determinant approaches the threshold, effectively imposing an energetic resistance to element collapse or inversion.

As illustrated in Fig. 3, this behavior is conceptually analogous to embedding a virtual nonlinear spring system within each finite element. These virtual springs remain dormant when the element shape is healthy but exhibit rapidly increasing stiffness as the local volume shrinks abnormally or approaches singularity. Instead of altering the physical equilibrium forces, this formulation induces a localized stiffening effect that effectively arrests excessive distortion without altering the physical response of feasible regions. Consequently, the barrier function ensures that the mapping from the reference to the deformed configuration remains well behaved, making the method particularly suitable for robust large-deformation analysis.

3.3 Multiresolution nonlinear isogeometric topology optimization

This hierarchical structure enables a clear separation between analysis and design, which is central to the multiresolution paradigm. It significantly reduces the number of analysis degrees of freedom by using a coarse analysis mesh, while still capturing fine structural details through the high-resolution density mesh used for design updates. The coarser analysis meshes are mapped to the fine design mesh via NURBS interpolation schemes, ensuring consistent information transfer. The multiresolution density mapping formula is given by

$$\tilde{\rho}_{\zeta}^{e} = \frac{1}{\ell_{\zeta}(e)} \sum_{i \in \ell_{\zeta}(e)} \rho_i, \tag{26}$$

where $\tilde{\rho}_{\zeta}^{e}$ denotes the density at the Gauss integration point ζ within the coarse element e, used for nonlinear IGA. ℓ_{ζ} represents the set of fine elements in the neighborhood of the integration point.

For the multiresolution nonlinear topology optimization problem, Eq. (17) should be corrected as

$$\begin{aligned} &\min_{0 \le \rho_e \le 1} : C(\boldsymbol{\rho}) = \boldsymbol{L}^{\mathrm{T}} \boldsymbol{u}_{\varphi} \\ &\text{s.t.} : \boldsymbol{R}_{\varphi}(\boldsymbol{\rho}, \boldsymbol{u}_{\varphi}) = \boldsymbol{0} \\ &g = \sum_{e=1}^{n_e} \rho_e v_e - V \le 0 \end{aligned}, \tag{27}$$

where the displacement vector $\boldsymbol{u}_{\varphi}$ corresponding to the optimization mesh is obtained by interpolating the displacement $\boldsymbol{u}$ from the analysis mesh:

$$\boldsymbol{u}_{\varphi} = \sum_{A=1}^{n_c} R(\xi_{\varphi}, \eta_{\varphi}) \boldsymbol{u}, \tag{28}$$

where $(\xi_{\varphi}, \eta_{\varphi})$ is the knot vector corresponding to the optimization mesh.

The sensitivity of the objective function can be derived using the Lagrange multiplier method:

$$\frac{\partial C}{\partial \rho_e} = -\boldsymbol{\vartheta}^{\mathrm{T}} (\alpha \rho_e^{\alpha-1} E_0) \boldsymbol{f}_{\mathrm{int}}^{\varphi}(\xi_{\varphi}, \eta_{\varphi}), \tag{29}$$

where $\boldsymbol{f}_{\mathrm{int}}^{\varphi}$ is the internal force vector on the optimization mesh.

3.4 Automated adaptive resolution method

To further enhance computational efficiency while preserving the ability to capture fine structural details, this paper proposes an automated adaptive resolution method. Unlike conventional multiresolution approaches with fixed-resolution ratios, the proposed method dynamically adjusts analysis mesh resolution based on the convergence trend and objective-based QR-patterns detection algorithm during the optimization process, as illustrated in Fig. 4.

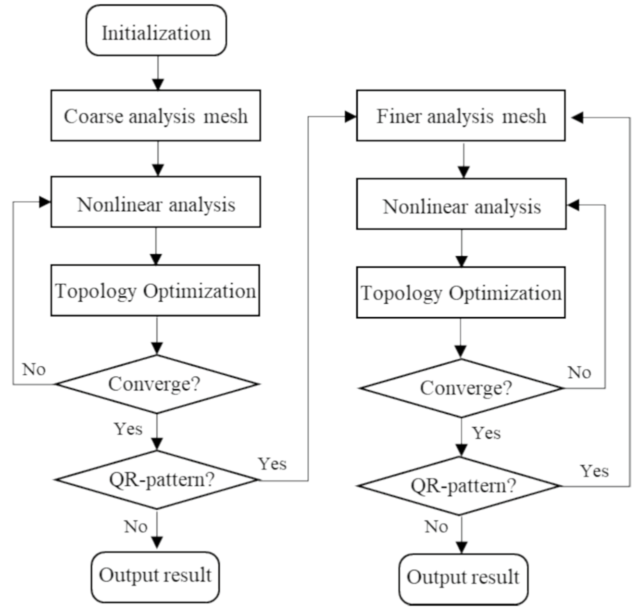

Fig. 4 The flowchart of the automated adaptive resolution method

At the early stages of optimization, a coarse mesh is adopted to reduce computational costs and accelerate the convergence of the global structural layout. The convergence is determined according to the predefined objective convergence criterion. If the criterion is not satisfied, the optimization iterations continue. Once convergence is achieved, the objective-based QR-patterns detection algorithm will be activated. If the detection criterion is not satisfied, the current topology result is output. Otherwise, a finer analysis mesh is adopted to continue the optimization iterations until the final topology result is obtained.

To implement the automated adaptive resolution method, a convergence criterion for the objective function must be predefined, i.e., the relative change of the objective function over the most recent iterations should be smaller than a specified threshold. Therefore, we first define a historical sequence of the objective function:

$$\{C^{(k)}\} = \{C^{(1)}, C^{(2)}, \ldots, C^{(n)}\}, \tag{30}$$

where $C^{(k)}$ is the objective function value at iteration k. We then compute the sequence of relative changes over the most recent N steps (with $N=5$ in this paper):

$$\Delta^{(k)} = \frac{\left|C^{(k)} - C^{(k-1)}\right|}{C^{(k-1)}} (k = n - N + 1, \ldots, n), \tag{31}$$

that is, the relative change rate of the objective function between successive iterations over the most recent N steps. Furthermore, the maximum relative change rate is computed.

$$\Delta_{\max} = \max(\Delta^{(n-N+1)}, \ldots, \Delta^{(n)}), \tag{33}$$

Subsequently, when $\Delta_{\max}$ is lower than the threshold ε (with $\varepsilon = 0.005$ in this paper), the objective-based QR-patterns detection algorithm is activated. The core idea of this algorithm is to perform an additional analysis using a finer mesh in the current optimization iteration and compute the corresponding objective function value. If the relative change between the objective function obtained on the finer mesh and the current objective function remains below the threshold, the optimization is considered converged. Otherwise, the method automatically switches to the finer analysis mesh to continue the optimization process. The judgment criterion is as follows:

$$\frac{\left|C_{finer} - C^k\right|}{C^k} > \varepsilon, \tag{34}$$

where C_{finer} denotes the objective function value computed on the finer mesh.

3.5 Optimization design and post-processing workflow

Figure 5 illustrates the complete workflow of the proposed multiresolution nonlinear isogeometric topology optimization and post-processing method, which can be divided into three stages. Stage 1: Nonlinear IGA. First, based on the NURBS representation, the structural geometry and analysis domain are constructed. After applying boundary conditions, loads, and material parameters, nonlinear isogeometric analysis is performed using a coarse analysis mesh to reduce computational cost. Stage 2: Multiresolution topology optimization. During the topology optimization stage, a fine optimization mesh is used to design the material layout. Sensitivity analysis and optimization algorithms are employed to iteratively update the material distribution. The analysis and density mesh are decoupled: the coarse mesh is used for structural analysis, while the fine mesh describes the design variables, thus balancing computational

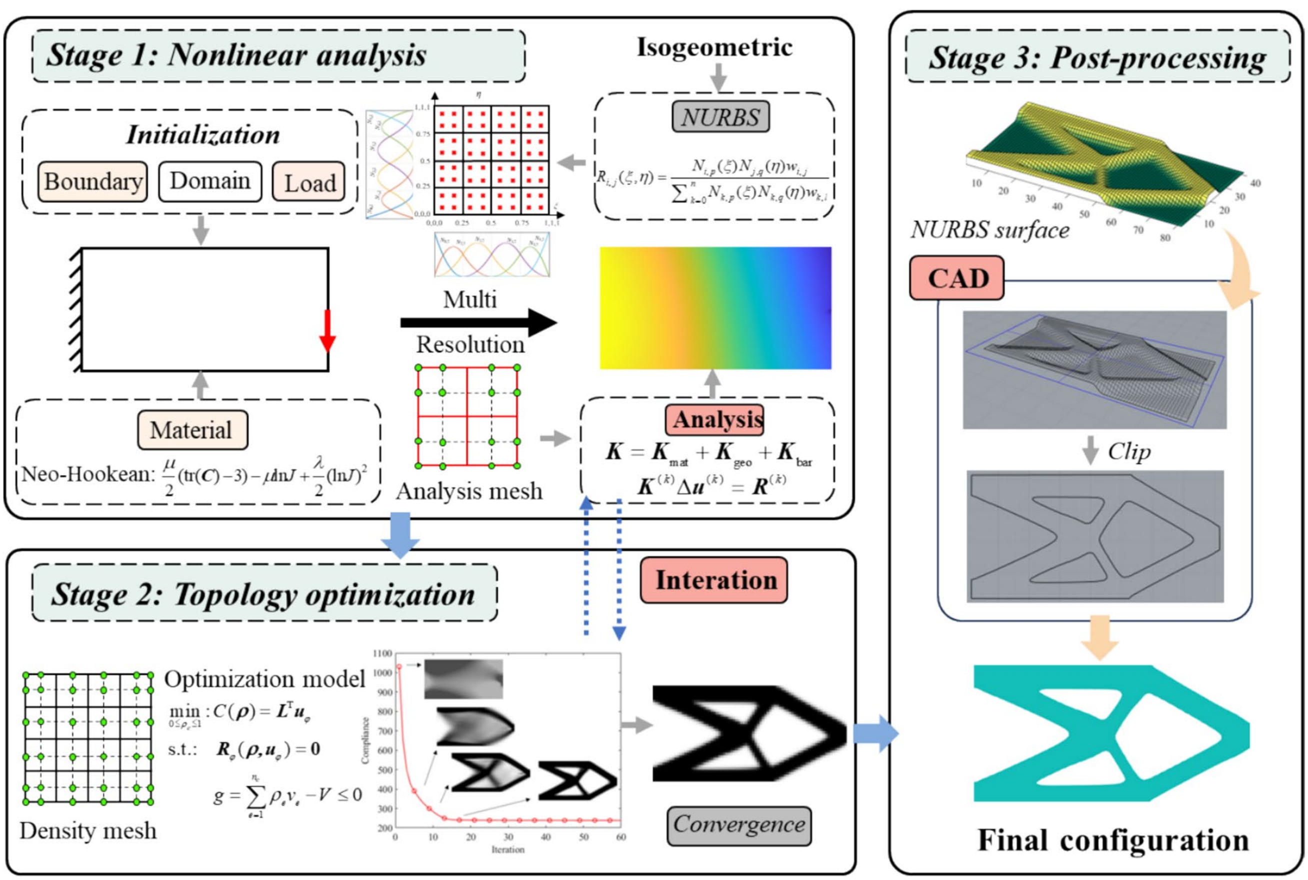

Fig. 5 Topology optimization process and post-processing diagram

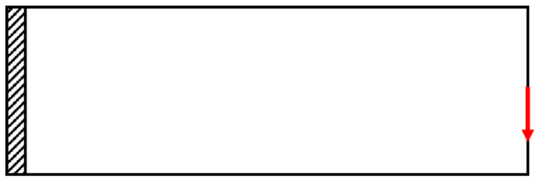

Fig. 6 Schematic of the cantilever beam

efficiency and design resolution as explained in Sect. 3.5. Stage 3: Post-processing and CAD model generation. Leveraging the inherent geometric continuity of the isogeometric framework, the optimized topology is naturally represented as a NURBS surface, facilitating a seamless transition to editable CAD models. Unlike conventional element-based approaches that suffer from boundary ambiguity, the proposed workflow exports the density field as a NURBS surface via standard IGES formats. In the CAD environment, a horizontal threshold plane is constructed to intersect with this density surface, acting as a precise geometric filter. The height of the threshold plane is determined through an iterative calibration process to approximate the target volume constraint. By computing the intersection curves between the smooth NURBS surface and the cutting plane, error-free boundary contours are extracted to reconstruct the final solid geometry. This method effectively eliminates the jagged edges typical of grayscale elements, enabling the rapid generation of precise, editable CAD models for direct engineering application.

4 Benchmark

To systematically evaluate the performance of the proposed automated adaptive resolution topology optimization method, a benchmark cantilever beam problem is investigated in this section. The study focuses on assessing how the multiresolution strategy influences nonlinear analysis accuracy, structural topology representation, and computational efficiency. Specifically, four aspects are explored: 1. The impact of different analysis meshes on the convergence of nonlinear analysis and resulting topology; 2. The role of filter radius in controlling the resolution of structural features; 3. The effectiveness of the proposed automated adaptive resolution method in balancing design quality and computational cost; 4. The influence of mesh density on the overall performance of multiresolution optimization. All simulations are conducted on a desktop computer equipped with a 12th Gen Intel(R) Core (TM) i7-12700F 2.10 GHz CPU and 16 GB of RAM.

The schematic of the cantilever beam is shown in Fig. 6, with a design domain of 120 mm × 40 mm with 1 mm × 1 mm elements. The beam is fixed at the left end, with a downward load $F = 10$ N applied at the midpoint of the right end. The structure is modeled using a compressible Neo-Hookean material, with a Young's modulus of 300 MPa and a Poisson's ratio of 0.4. The volume fraction and SIMP penalty factor are set to 0.5 and 3, respectively. In the nonlinear analysis, the load increment number is set to 10, with a convergence tolerance $e_{tol} = 10^{-3}$, and the number of Newton–Raphson iterations is capped at 10 per load step. The termination criterion for optimization iterations is set to 10^{-5}.

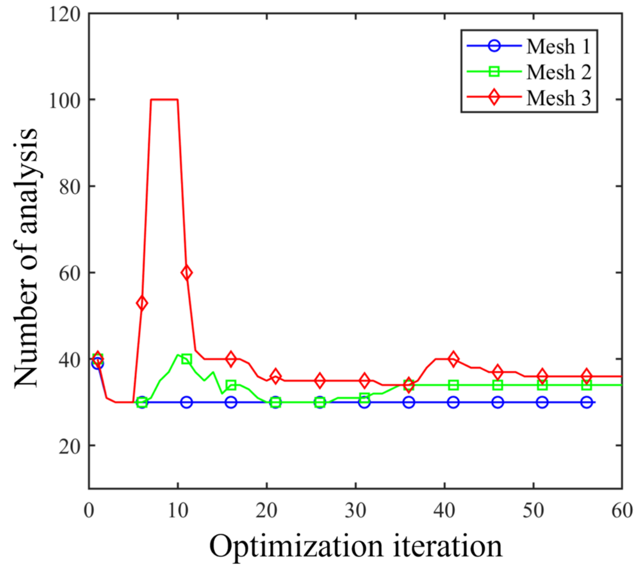

Fig. 7 Convergence curves of nonlinear analysis step during optimization

4.1 Effect of analysis mesh

This subsection investigates the impact of the analysis mesh on the convergence behavior of nonlinear analysis and the resulting topology. The filter radius is set to 1.5 mm. Mesh 1, Mesh 2, and Mesh 3 are examined, and the corresponding numbers of DoF are 10,248, 2728 and 768, respectively.

Figure 7 presents the convergence history of the nonlinear analysis in terms of the number of Newton–Raphson analyses per optimization step. When using Mesh 1, the number of nonlinear analyses rapidly stabilizes at around 30, corresponding to approximately 3 iterations per load increment. For Mesh 2, minor fluctuations are observed, but convergence is achieved after about 34 optimization iterations. However, in Mesh 3, significant oscillations occur in the early optimization phase. This instability is primarily due to the coarse analysis mesh, which lacks sufficient accuracy to accommodate rapid changes in design variables, thereby hindering the convergence of the nonlinear analysis. As the

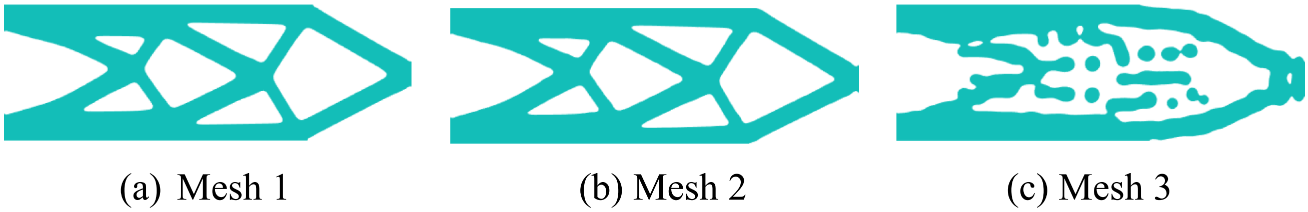

Fig. 8 Post-processed topologies under different analysis meshes

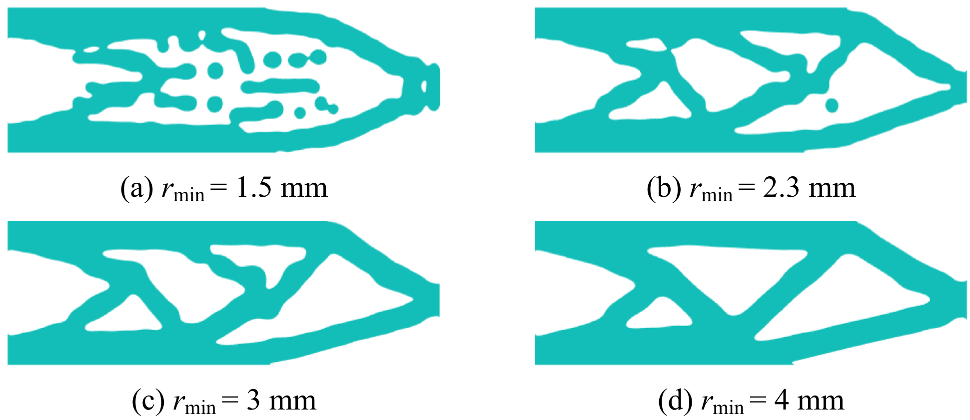

Fig. 9 Post-processed topologies under different filter radii

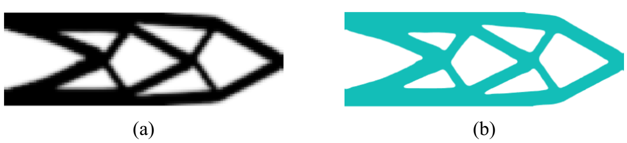

Fig. 10 Optimized configurations, **a** topology, **b** post-processed

design stabilizes, the nonlinear solver gradually regains convergence.

Figure 8 displays the post-processed topologies corresponding to the three mesh resolutions. The results for Mesh 1 and Mesh 2 exhibit highly consistent structural layouts. In contrast, the Mesh 3 case shows irregular transitions and islanding phenomenon, which are attributed to an insufficient filter radius relative to the fine design mesh. This leads to overly sharp local variations and poor structural regularity. A commonly adopted remedy is to appropriately increase the filter radius to mitigate these issues.

4.2 Effect of filter radius

To further evaluate the influence of filter radius under a fine-resolution setting, we investigate the topologies generated with Mesh 3 using four different filter radii $r_{\min} = 1.5$ mm (for baseline comparison), 2.3 mm, 3 mm, and 4 mm. The post-processed topologies are shown in Fig. 9.

The results demonstrate that increasing the filter radius effectively suppresses the previously observed irregular transitions and islanding feature. However, this improvement comes at the cost of over-smoothing, which may eliminate slender members or other fine-scale features. This trade-off can negatively impact design fidelity, particularly in applications requiring high geometric complexity and resolution.

4.3 Optimization of the automated adaptive resolution method

To address the challenges observed in the previous sections, we adopt the automated adaptive resolution method described earlier to achieve the adaptive mesh switching. The process begins with Mesh 3 for initial optimization. Once the objective function satisfies the predefined convergence criterion, the compliance-based QR-pattern detection algorithm is activated. If QR-patterns are detected, the analysis mesh is automatically switched to the finer-resolution Mesh 2 to continue the optimization process. It is worth noting that the filter radius remains fixed at 1.5 throughout this example. As shown in Fig. 10, the final optimized and post-processed topologies obtained using this strategy are nearly identical to those obtained under Mesh 1 and Mesh 2, demonstrating the structural consistency and reliability of the adaptive approach.

To better illustrate the transition process, Fig. 11a presents the evolution of the objective function and the

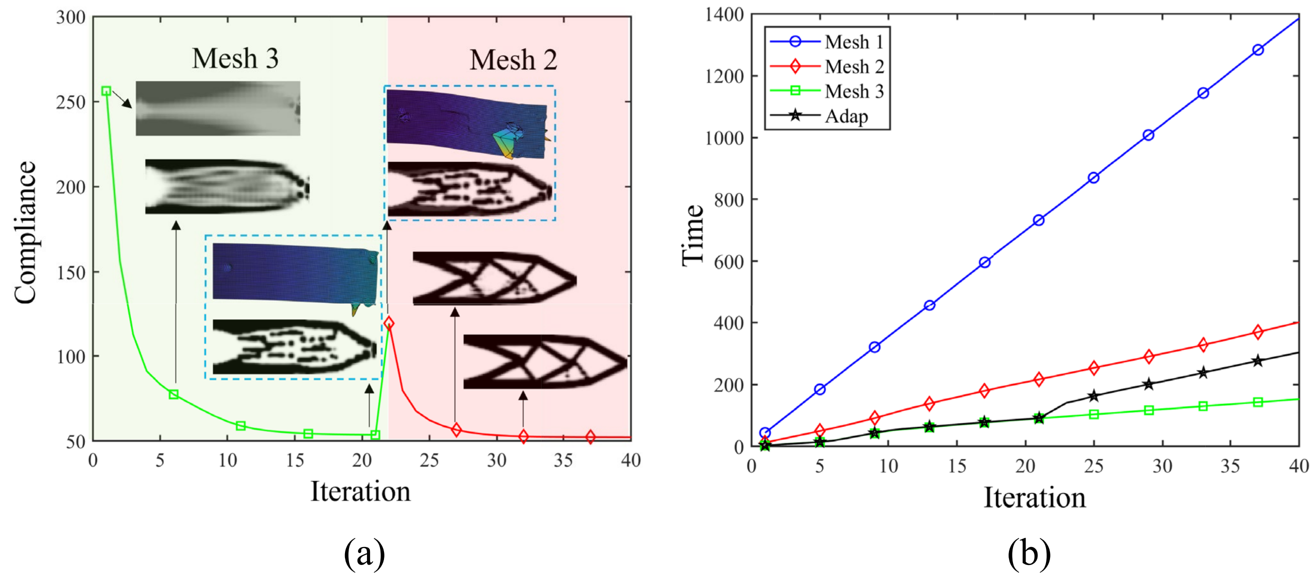

Fig. 11 Iterative curves, **a** compliance, **b** time

corresponding topology during optimization. The green and red lines denote the iteration curves for the Mesh 3 and Mesh 2 resolution stages, respectively. As shown in Fig. 11a, a noticeable spike in compliance occurs at Iteration 22. This phenomenon is attributed to the release of artificial stiffness caused by the mismatch between the fixed small filter radius and the coarse analysis mesh. The coarse elements artificially bridge the discontinuous material islands formed by the small filter, leading to stiffness overestimation. When switching to the finer Mesh 2, this artificial constraint is removed, resulting in a sudden increase in compliance. This mechanism is visually corroborated by the displacement contours presented in the insets of Fig. 11a, which clearly show a significant increase in structural displacement. Such a sudden increase in displacement accompanied by mesh distortion inevitably leads to an abrupt jump in compliance, which clearly poses a risk of divergence for extremely nonlinear problems. However, accounting for the variation of the filtering radius during multiresolution mesh transitions can effectively alleviate the aforementioned issue. The detailed discussion will be provided in Sect. 4.4.

In addition, Fig. 11b compares the total computational time for different multiresolution settings: Mesh 1, Mesh 2, Mesh 3 and the adaptive mesh (Mesh 3 → Mesh 2). The total optimization times are 1385 s, 400 s, 153 s, and 307 s, respectively. The corresponding speed-up rates of the multiresolution schemes compared to Mesh 1 are 71.12%, 88.95%, and 77.83%. These results clearly demonstrate that the automated adaptive resolution method achieves substantial improvements in computational efficiency while maintaining the structural quality and detail of the final design.

4.4 Effect of element discretization scale and filter radius switching scheme

To further evaluate the influence of finer mesh discretization on nonlinear topology optimization using the automated adaptive resolution method, we consider a refined design density mesh of 240 mm × 80 mm. The multiresolution meshes and corresponding filter radii are set as follows, Case1: Mesh 1 with 1.5 mm, Case2: Mesh 2 with 1.5 mm, Case 3: Mesh 3 with 3 mm, Case 4: Mesh 4 with 6 mm, Case 5: Adaptive mesh (Mesh 4 → Mesh 3) with 3 mm, Case 5: Adaptive mesh (Mesh 4 → Mesh 3) with 3 mm, Case 6: Adaptive mesh (Mesh 4 → Mesh 3) with 6 mm → 3 mm, Case 7: Adaptive mesh (Mesh 4 → Mesh 3 → Mesh 2) with 1.5 mm, Case 8: Adaptive mesh (Mesh 4 → Mesh 3 → Mesh 2) with 6 mm → 3 mm → 1.5 mm.

The post-processed topologies under different resolutions are shown in Fig. 12. It can be observed that all configurations, except for the Mesh 4 case, produce reasonable and smooth boundary topologies. It is also proved that the element discretization scale significantly affects the selection of a suitable analysis mesh. For instance, Mesh 3 is feasible under the discretization of 240 mm × 80 mm but not 120 mm × 40 mm. Furthermore, applying an automated adaptive multiresolution method by switching from Mesh 4 to Mesh 3 effectively resolves the discontinuities observed in the Mesh 4 resolution case.

Crucially, the comparison between fixed and filter radius switching schemes reveals a fundamental insight into the multiresolution process. Comparing Case 5 and Case 6 or Case 7 and Case 8 offers the most significant finding. In Case 5 and Case 7, an automated adaptive mesh scheme is

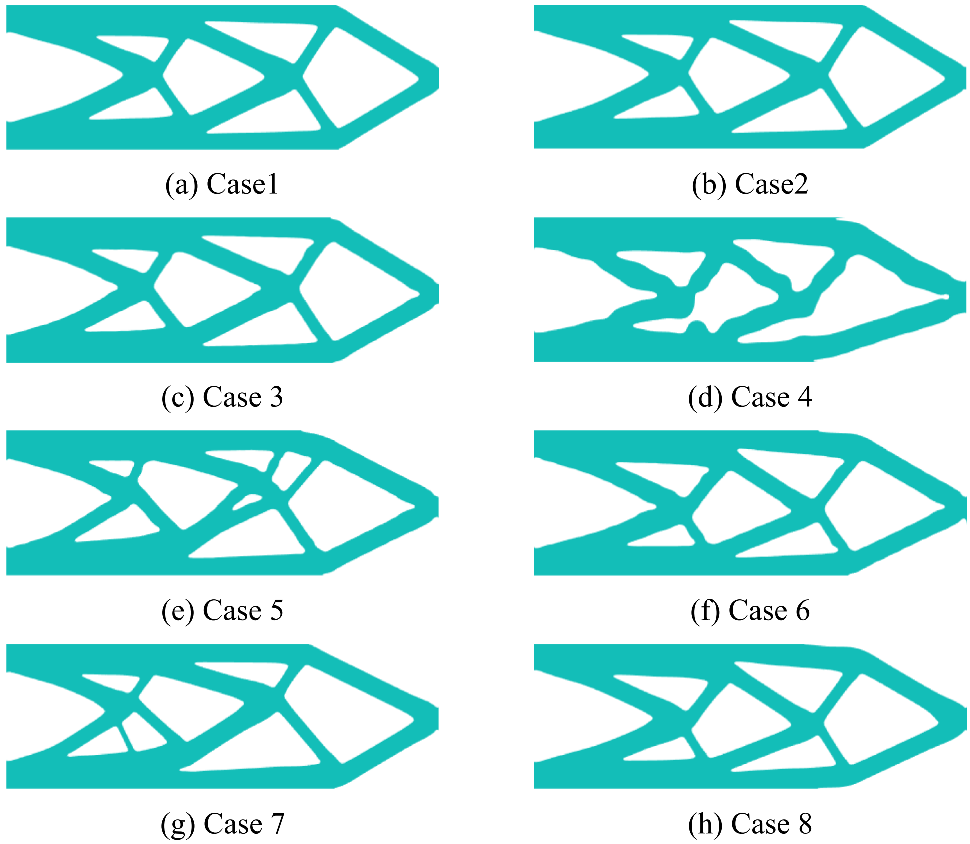

Fig. 12 Post-processed configurations of the optimized solutions for different analysis mesh resolutions and filter radii

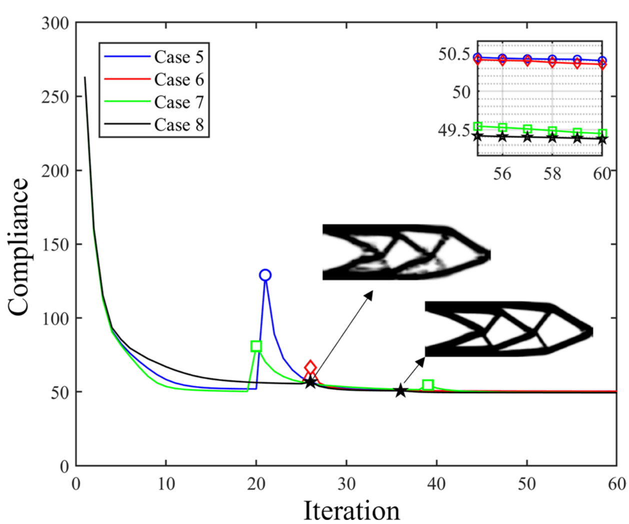

Fig. 13 Iterative curve of the objective function and the topology configurations of Case 8 at the mesh transition stages

employed but with a fixed small filter radius throughout. It can be observed that the final topologies exhibit additional thin struts in the branching region. This is attributed to the mismatch between the small filter radius and the coarse elements during the early optimization stages (Mesh 4). The small filter fails to suppress QR-patterns in the coarse mesh, causing the optimizer to converge prematurely to a local optimum, which are difficult to remove even after subsequent mesh refinement. In contrast, Case 6 and Case 8 adopt a coupled adaptive strategy, where the filter radius decreases synchronously with mesh refinement. This topology continuation approach ensures that a coherent global structure is established early using a large filter, while fine features are progressively resolved as the mesh and filter are refined. Consequently, Case 6 and Case 8 produce topologies that are remarkably consistent with the high-resolution baseline (Case 1), effectively eliminating the discontinuities found in Case 4 and the thin strut observed in Case 7.

Figure 13 presents the compliance histories as well as the topology configurations of Case 8 at the two mesh transition stages. It can be clearly observed that noticeable compliance jumps occur in Case 5 and Case 7 during mesh transitions. As discussed above, this behavior is mainly attributed to the mismatch between a small filtering radius and coarse elements. When the filtering radius is adjusted with the mesh transitions, as in Case 6 and Case 8, the compliance fluctuations become much less pronounced. This observation further explains the mesh-induced oscillations shown in Fig. 11a. From the perspective of the final structural compliance, the cases with two mesh transitions (Case 7 and Case 8) exhibit better performance than those with only one mesh transition (Case 5 and Case 6). Moreover, the cases in which

Fig. 14 The schematic of the cantilever beam

the filtering radius varies with the multiresolution mesh outperform those using a fixed filtering radius, indicating that accounting for the variation of the filtering radius is necessary in the automated adaptive resolution method.

Overall, the differences in the final compliance values among the four cases are not significant, all of them effectively avoid the mesh discontinuity issues observed in Case 4, which further demonstrates the necessity and robustness of the proposed automated adaptive resolution method.

5 Numerical examples

To further validate the applicability and superiority of the h-refinement multiresolution and stable nonlinear isogeometric topology optimization method in practical engineering scenarios, this section presents numerical studies on representative structural examples. The designs comprehensively incorporate key considerations, including the automated adaptive resolution method, and the self-adjusting barrier regularization method. The primary objective is to evaluate the method's overall performance in mitigating mesh distortion, preserving structural topology quality, and improving computational efficiency.

5.1 Cantilever beam

The cantilever beam example is used to validate the effectiveness of the self-adjusting barrier regularization method within the multiresolution framework. The geometry, loading, and boundary conditions of the cantilever beam are illustrated in Fig. 14. The design domain is discretized into a design density mesh of 122 mm × 32 mm elements. The structure is modeled using a compressible Neo-Hookean material with Young's modulus $E = 300$ MPa and Poisson's ratio $\nu = 0.4$. The threshold for the barrier regularization term is set to $\delta = 10^{-5}$.

In the nonlinear analysis, the load increment number is 10, with a convergence tolerance $e_{tol} = 10^{-3}$, and the number of Newton–Raphson iterations is limited to 5 per step. The

Table 2 Comparison of topology and mesh configurations, structural compliance, analysis steps, and optimization time under different loads

	Non-barrier	Hybrid constitutive	SA-barrier
$F = 1$ N	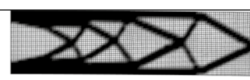	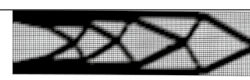	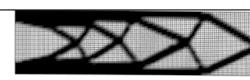
C - A -T	0.99-1205-422	0.99-1290-423	0.99-1238-436
$F = 10$ N	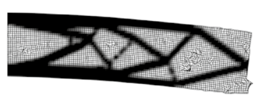	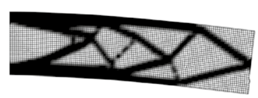	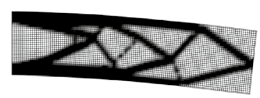
C - A -T	9.89-1978-658	9.89-1463-481	9.89-1446-514
$F = 20$ N	/	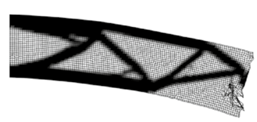	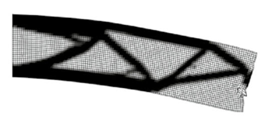
C - A -T	/	392.4-2225-695	392.9-2316-785
$F = 30$ N	/	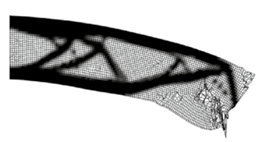	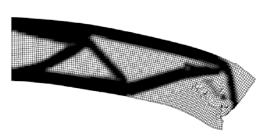
C - A -T	/	876.2-3683-1156	870.8-2667-880
$F = 35$ N	/	/	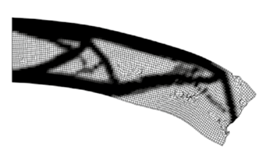
C - A -T	/	/	1217-3105-1085

volume fraction, filter radius, and SIMP penalty factor are set to 0.5, 1.5 mm, and 3, respectively. Multiresolution starting with Mesh 2 is employed.

Under different loading conditions, the results of the topology and mesh configurations are compared between the non-barrier method (without barrier), the Hybrid constitutive method (low-density elements adopt linear elastic constitutive model, high-density elements adopt Neo-Hookean material model) and the SA-barrier method. Consistent with the hybrid constitutive method, the linear elements employed in the low-density regions utilize the same material parameters to ensure physical continuity in the small-strain regime. Key performance metrics, including structural compliance (C), total analysis number (A), and total optimization time (T), are summarized in Table 2.

As presented in Table 2, under small loads ($F=1$ N), the three methods produce consistent topologies and structural compliance. Regarding computational efficiency, the non-barrier method requires the fewest analysis iterations. While the Hybrid constitutive method introduces a slight increase in iterations due to the coupling of linear and nonlinear elements, the use of linear theory in void regions reduces the cost per equilibrium step. Consequently, its total optimization time remains comparable to the non-barrier method. The SA-barrier method incurs a minor computational overhead due to the barrier terms, resulting in slightly higher iteration counts and time under this small-deformation scenario.

When the load increases to $F=10$ N, consistent topologies are still maintained, but the non-barrier method begins to exhibit noticeable mesh distortion. This phenomenon occurs because, in the conventional non-barrier formulation, low-density elements possess negligible stiffness and offer little resistance to nodal drift, allowing them to undergo excessive, non-physical deformations even under moderate loads. Crucially, this distortion negatively impacts numerical performance: the non-barrier method requires significantly more analysis steps (1978) and time (658 s) compared to the SA-barrier method (1446 steps / 514 s). The efficiency advantage of the SA-barrier method stems from its underlying regularization mechanism: the barrier function acts as a mesh-quality-dependent energy potential that grows asymptotically as the Jacobian determinant approaches zero. This induces a localized stiffening effect that effectively arrests element collapse without altering the physical equilibrium forces of feasible regions, thereby maintaining a healthy discretization and improving the conditioning of the equilibrium iterations. As the load reaches $F=20$ N, the non-barrier method fails due to the breakdown of the nonlinear analysis (Jacobian singularity) triggered by element inversion ($J \leq 0$). The Hybrid constitutive and SA-barrier methods continue to function.

At high load levels ($F=30$ N and $F=35$ N), the performance gap widens. At $F=30$ N, the Hybrid constitutive method maintains baseline stiffness in low-density regions, smoothing the deformation. However, comparing the structural compliance and computational cost in Table 2 reveals that the SA-barrier method achieves a similar compliance with significantly reduced computational cost (Time: 880 s vs. 1156 s for Hybrid constitutive). Furthermore, at the extreme load of $F=35$ N, the Hybrid constitutive method fails to converge, whereas the

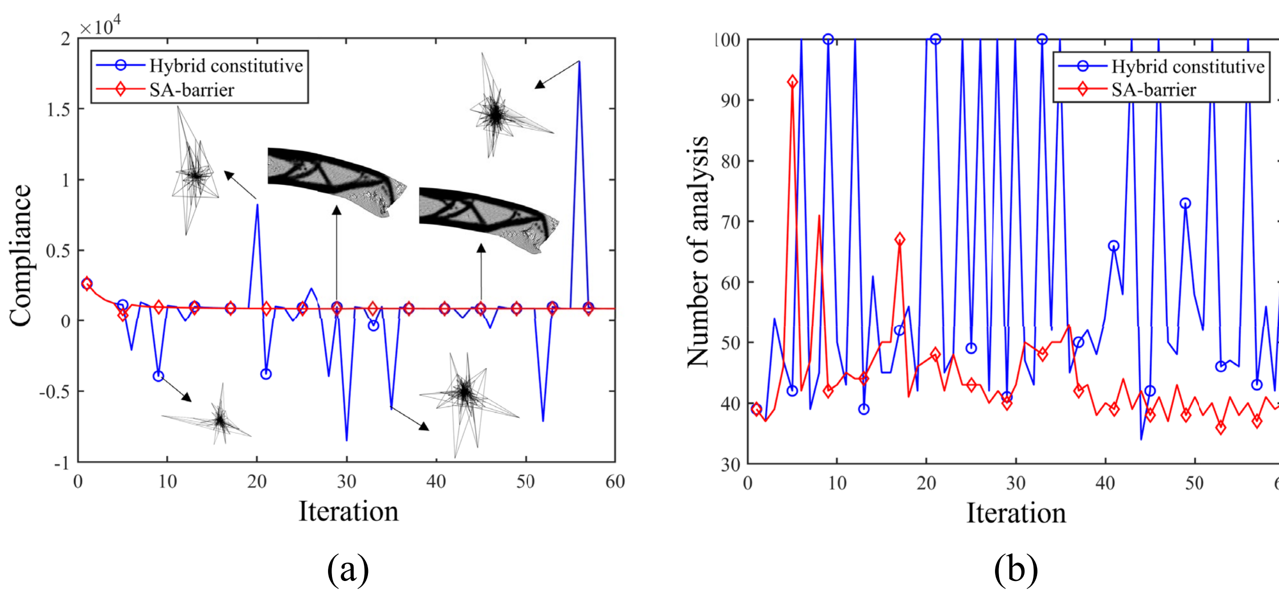

Fig. 15 Iteration curves, **a** compliance and topology configurations of the Hybrid constitutive method; **b** number of nonlinear analysis

SA-barrier method successfully generates a valid design. This demonstrates that the SA-barrier method, by penalizing near-singular deformations via stiffness regularization, offers a superior stability margin. The numerical behavior under $F = 30$ N is further elucidated in Fig. 15. The compliance history (Fig. 15a) shows that the Hybrid constitutive method suffers from pronounced oscillations (blue line), with spikes corresponding to intermittent mesh distortions shown in the inset images. These distortions imply that the optimizer temporarily traverses infeasible geometric configurations. In contrast, the SA-barrier method (red line) exhibits a smooth and stable convergence trend. This robustness is corroborated by the analysis iteration history (Fig. 15b), where the SA-barrier method maintains a consistently lower number of Newton iterations (around 40–50), preventing the numerical deterioration observed in the Hybrid constitutive method.

5.2 Curved beam

To demonstrate the advantages of NURBS in accurately representing complex or arbitrarily shaped geometries, as well as to further showcase the feasibility and benefits of the proposed automated adaptive resolution framework with self-adjusting barrier regularization for stable nonlinear isogeometric topology optimization, a curved beam with a quarter-ring geometry is considered, as shown in Fig. 16a. The bottom edge of the beam is fully fixed, and a horizontal load $F = 10$ N is applied at the top-left corner.

The initial control mesh of the beam is presented in Fig. 16b. The design density mesh is 160 mm × 80 mm, as illustrated in Fig. 16c, where black represents density meshes and red denotes analysis meshes (corresponding to Mesh 2). The material model follows the compressible Neo-Hookean formulation, with Young's modulus and Poisson's ratio set to 300 MPa and 0.4, respectively. The volume fraction and SIMP penalty factor are set to 0.5, and 3, respectively. In each optimization iteration, the load increment number is 10. The nonlinear analysis uses a convergence tolerance $e_{tol} = 10^{-3}$, with the Newton–Raphson solver capped at 5 iterations per load increment.

To investigate the performance of the multiresolution strategy in nonlinear problems, five multiresolution mesh cases are considered, Case 1: Mesh 1with filter

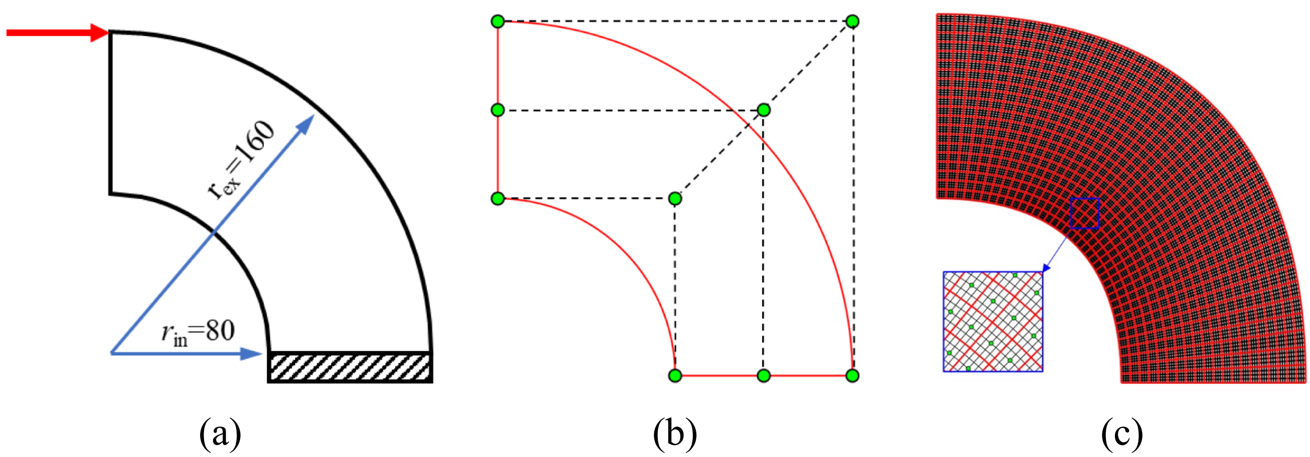

Fig. 16 Curved beam, **a** the design domain, **b** the initial control point mesh, and **c** the discretized density and analysis mesh

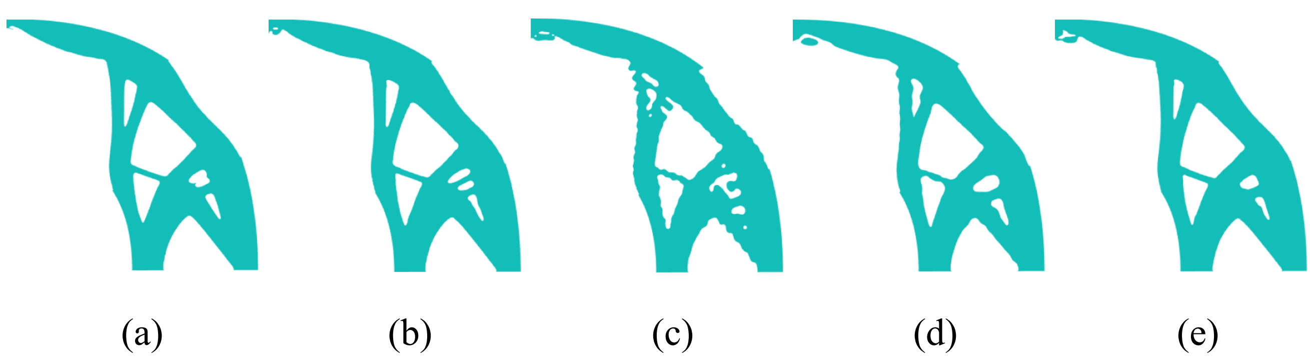

Fig. 17 The post-processed topologies, **a** Case 1, **b** Case 2, **c** Case 3, **d** Case 4, **e** Case 5

Table 3 Computational performance with different analysis mesh resolutions

	Mesh 1 $r_{\min}=1.5$	Mesh 2 $r_{\min}=1.5$	Mesh 3 $r_{\min}=1.5$	Mesh 3 $r_{\min}=3$	Adaptive mesh $r_{\min}=3\rightarrow1.5$
DoFs	26,568	6888	1848	1848	1848 → 6888
Compliance	17.79	17.44	17.24	17.52	17.60
Time/s	5026	1345	536	403	862
Time Saving/%	/	73.2%	89.3%	92.0%	82.9%

radius $r_{\min}=1.5$, Case 2: Mesh 2 with filter radius $r_{\min}=1.5$, Case 3: Mesh 3 with filter radius $r_{\min}=1.5$, Case 4: Mesh 3 with filter radius $r_{\min}=1.5$, and Case 5: the adaptive mesh of the automated adaptive resolution method with filter radius $r_{\min}=3\rightarrow1.5$. The post-processed topologies are shown in Fig. 17.

The main load-bearing paths are consistent across all analysis mesh resolutions, indicating that the multiresolution method maintains strong robustness in preserving global structural features. However, Case 3 exhibits distinct irregular transition features, primarily attributed to the mismatch between the coarse analysis mesh and the fine density mesh coupled with an excessively small filter radius. When a larger filter radius is employed, as in Case 4, these issues are partially mitigated; nevertheless, the boundary smoothness remains unsatisfactory, and islanding artifacts are observed. In contrast, Case 5 utilizes the automated adaptive resolution method (transitioning from Mesh 3 to Mesh 2 with R = 3 → 1.5), which effectively resolves these problems, yielding a smooth and refined topology comparable to the finer Case 1.

Table 3 summarizes the computational performance metrics under different cases, including: the number of DoF in the analysis mesh, the final structural compliance, total optimization time, and the corresponding efficiency improvement compared to the solution using Mesh 1. The four cases achieve efficiency improvements of approximately 73.2%, 89.3%, 92.0%, and 82.6%, respectively. Moreover, the compliance difference between Case 5 and Case 1 is the smallest. These findings further demonstrate that the automated adaptive resolution method effectively enhances optimization efficiency while preserving both the topological configuration and structural performance.

In addition, Fig. 18 presents the iteration histories of structural compliance and volume fraction. The structure converges rapidly and smoothly within 20 iterations, and the volume fraction consistently remains at the prescribed constraint of 0.5, demonstrating the proposed method's strong convergence and volume preservation in nonlinear settings. It is also observed that at the 20th iteration, accompanied by the filter radius switch, Case 5 does not exhibit the sudden spike seen in Fig. 11a. Instead, the compliance showed only minor fluctuations. This further indicates the necessity of

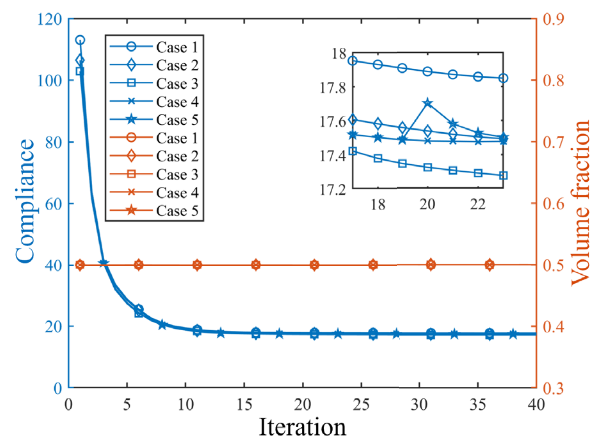

Fig. 18 Iterative curves of compliance and volume fraction

considering filter radius transitions in the automated adaptive resolution method.

Furthermore, to demonstrate the stability and robustness of the proposed method under large deformations, the topology optimization of a curved beam under various loading conditions is investigated, using Case 5 as a representative example. Figures 19a-d illustrate the deformed mesh topologies under loads of $F = 10$, 50, 100, and 150 N, respectively, while Fig. 19e-h present the corresponding post-processed configurations. It can be observed that the mesh exhibits no significant distortion even under large deformations, thereby validating the effectiveness of the SA-barrier method. Moreover, the ability to obtain reasonable and smooth topological configurations under different loading scenarios further confirms the feasibility of the automated adaptive resolution method in large-deformation applications.

5.3 Compliant mechanism

To further validate the applicability and effectiveness of the proposed automated adaptive resolution framework with SA-barrier method in highly flexible structures, a classical compliant mechanism, the inverter, is selected. Due to the symmetry of the inverter mechanism (Bendsøe and Sigmund 2003), the design domain and boundary conditions are illustrated in Fig. 20, with a mesh resolution of 120 mm × 80 mm. In this setup, the top-left corner is defined

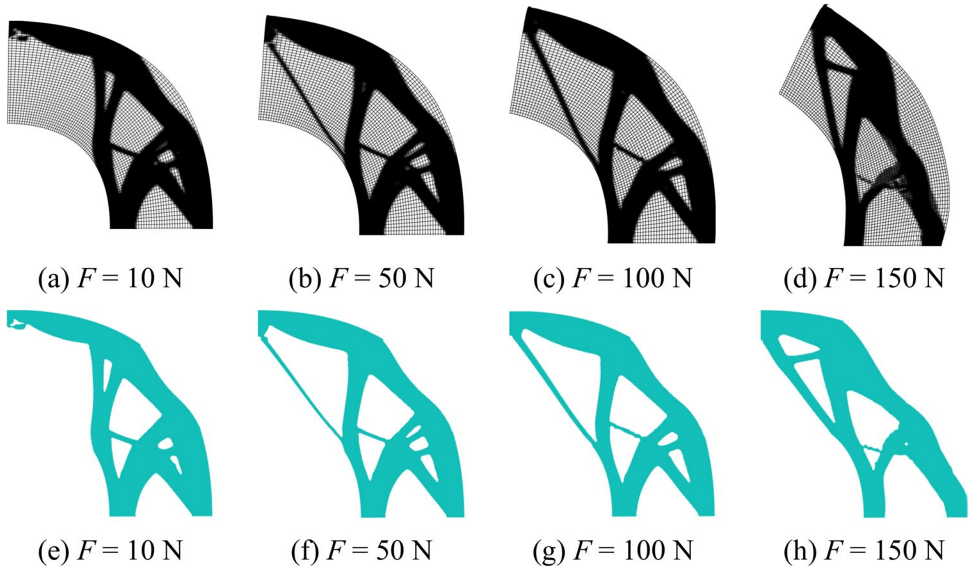

Fig. 19 Topological configurations under different loads, **a**–**d** mesh, **e**–**h** post-processed

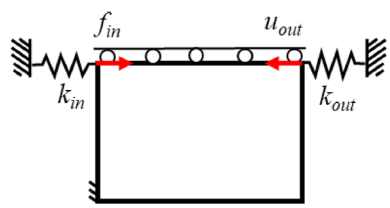

Fig. 20 Inverter mechanism

as the input point with an external force of 250 N and an attached spring of stiffness 10 N/mm. The objective is to maximize the displacement u_{out} for a given input force f_{in}. The top-right corner serves as the output point, where another spring of stiffness 10 N/mm is applied. The structure is modeled with Neo-Hookean material, with a Young's modulus of 3000 MPa and a Poisson's ratio of 0.4. The volume fraction and penalization factor are set to 0.25 and 3, respectively. For each optimization iteration, the load increment number is 10. The nonlinear analysis is governed by a convergence tolerance of $1e^{-3}$, and the Newton–Raphson iteration is limited to a maximum of 5 steps.

Table 4 presents the resulting mesh quality, topologies, and post-processed configurations under five cases, where Case 1 is Mesh 1 with filter radius $r_{\min} = 1.5$ under non-barrier, Case 2 is Mesh 2 with filter radius $r_{\min} = 1.5$ under non-barrier, Case 3 is Adaptive mesh (Mesh $2 \rightarrow 1$) with filter radius $r_{\min} = 1.5$ under non-barrier, Case 4 is Adaptive mesh (Mesh $2 \rightarrow 1$) with filter radius $r_{\min} = 1.5$ under SA-barrier and Case 5 is Adaptive mesh (Mesh $3 \rightarrow 2$) with filter radius $r_{\min} = 3 \rightarrow 1.5$ under SA-barrier. The corresponding output displacement (u_{out}) and optimization time (t_{opt}) are used to evaluate the performance. It is worth noting that in Case 1 and Case 3, if no additional small stiffness ($E_{\min}$) is introduced, the optimization process will fail to converge due to element singularities. Therefore, in this calculation example, $E_{\min} = 10^{-6}$ is specially set. In contrast, the SA-barrier method achieves stable optimization without requiring any such regularization, thereby maintaining better physical consistency.

As shown in Table 4, the optimized topologies obtained under Case 1, Case 2, Case 3, and Case 4 consistently exhibit a distinct dual-arm mechanism, with only minor variations in the maximum output displacement. Among them, Case 4 based on the automated adaptive resolution framework presents the topology and performance most similar to those of Case 1. In contrast, although Case 2, which considers only Mesh 2, outperforms Case 4 in terms of optimization time, its optimized topology, particularly in the hinge connection regions, shows noticeable deficiencies. This observation demonstrates the necessity of the automated adaptive resolution framework in compliant mechanism design.

It should be noted, however, that although Case 5 shows a significant improvement in optimization time, its resulting topology does not meet expectations. This is mainly because it adopts the coarsest mesh resolution (Mesh $3 \rightarrow 2$), which fails to accurately capture the local stiffness characteristics of the flexure hinge region, leading to numerical pseudo-flexibility issues such as single-node connections. This discretization error results in the poorest geometric clarity of the topology, and the displacement results deviate due to the underestimation of stiffness at the hinge. Therefore, in compliant mechanism optimization using the automated adaptive resolution method, the choice of the analysis mesh should be made carefully in accordance with the density mesh.

From the perspective of mesh quality, the SA-barrier method results in smoother and more natural mesh deformation, while the non-barrier approach suffers from severe

Table 4 Mesh quality, optimized topologies, post-processing configurations, and performance metrics of three cases

	Mesh	Topology	Post-processing
Case 1	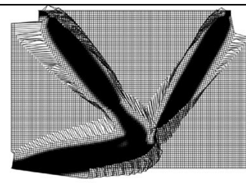		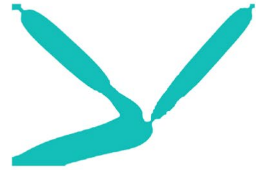
u_{out} - t_{opt}		–9.03 - 22818s	
Case 2	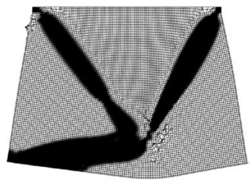		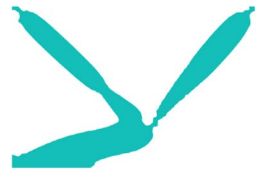
u_{out} - t_{opt}		–8.98 - 1219s	
Case 3	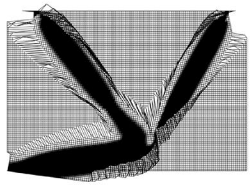		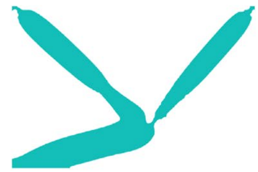
u_{out} - t_{opt}		–8.99 - 10435s	
Case 4	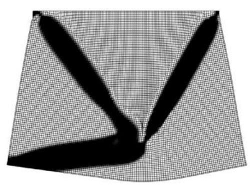		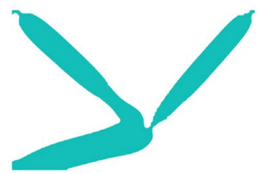
u_{out} - t_{opt}		–9.01 - 2011s	
Case 5	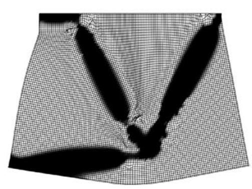		
u_{out} - t_{opt}		–9.17 - 683s	

mesh distortion. Additionally, Fig. 21 shows the iteration curves of analysis step number for the five cases. For Cases 2–4 that employ the resolution technique, the number of analysis iterations is relatively high in the early stage of optimization due to mesh effects. However, since the computations are initially performed on coarse meshes, the overall computational time remains low despite the larger number of iterations, leading to higher efficiency. In Case 5, the use of the coarsest Mesh 4 at the initial optimization stage results in the most pronounced fluctuations in the number of analysis iterations. After switching to Mesh 2, however, the incorporation of the SA-barrier method causes the analysis iterations to stabilize and eventually become consistent with those of Case 2 in the later stage. A comparison between Case 3 and Case 4 further reveals that, under the same automated adaptive resolution framework, Case 4 with the SA-barrier method exhibits smaller fluctuations in the early optimization stage and achieves the lowest iteration count in the later stage (31 iterations). This further demonstrates the advantages of combining the SA-barrier method with the automated adaptive resolution framework.

In summary, the self-adjusting barrier regularization technique not only ensures the accuracy of the optimized designs, but also significantly enhances the numerical

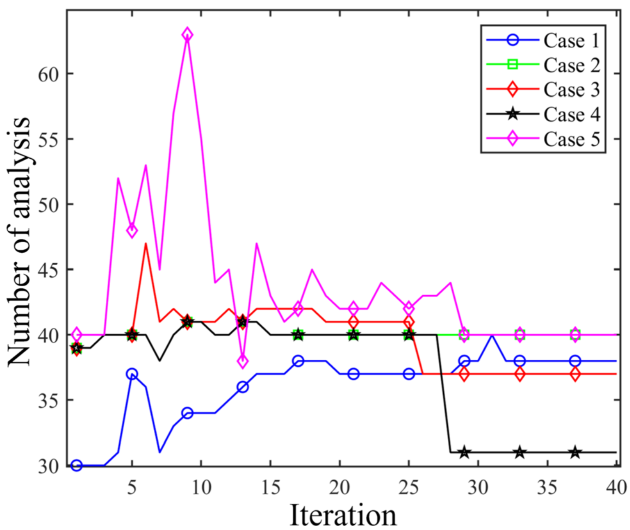

Fig. 21 Iterative curves of analysis step number

stability and computational efficiency in the topology optimization of compliant mechanisms. When integrated with the adaptive resolution strategy, the method achieves further computational savings, and the barrier term proves particularly effective in improving convergence behavior of the multiresolution framework under large-deformation conditions.

6 Conclusions

This study presents an automated adaptive resolution framework with self-adjusting barrier regularization for nonlinear isogeometric topology optimization. By integrating h-refinement-based adaptive resolution, Jacobian-based barrier regularization, and a NURBS-based post-processing strategy, the method achieves a favorable balance between accuracy, stability, and efficiency. The automated adaptive resolution method, guided by an objective-based QR-pattern detection algorithm, allows the framework to fully exploit the efficiency of coarse meshes in the early iterations and to switch to refined meshes once the objective stabilizes at the prescribed convergence threshold. This strategy effectively suppresses QR-patterns and significantly improves optimization efficiency.

The self-adjusting barrier regularization method further enhances stability of the multiresolution framework by preventing element distortion and Jacobian inversion under large deformation, eliminating the need for artificial parameters such as a minimum stiffness. Together, these features enable stable nonlinear analyses and improve optimization convergence, as demonstrated through benchmark and engineering-oriented numerical examples. The NURBS-based representation not only ensures geometric fidelity but also facilitates direct CAD export, bridging the gap between topology optimization and downstream manufacturing.

Overall, the proposed framework provides a stable and efficient solution approach for nonlinear topology optimization, particularly in applications involving large deformations and high geometric complexity. Although the core methodology is mathematically extensible to 3D continuum structures, specific challenges are anticipated. Firstly, regarding the self-adjusting barrier, the stabilization of complex 3D volumetric distortion modes (e.g., twisting or shear locking) may require re-calibration of the barrier parameters to balance regularization and physical accuracy. Secondly, the adaptive regulation of the filter radius becomes more sensitive in 3D; an improper adaptation law during mesh switching could exacerbate the resolution mismatch, potentially leading to topological disconnectivity or isolated material voids in the third dimension. Future work will focus on addressing these challenges and exploring more general physical scenarios, including nonlinear shell structures, contact problems, and multiphysics coupling, thereby broadening its applicability in advanced engineering design.

Acknowledgements Xinqing Li acknowledges the financial support by the China Scholarship Council program and the Young Elite Scientists Sponsorship Program by CAST – Doctoral Student Special Plan.

Yingjun Wang acknowledges the financial support by the Guangdong Basic and Applied Basic Research Foundation (2024A1515011786 and 2025A1515010672).

Author contributions Xinqing Li: Writing – original draft, Conceptualization, Methodology, Software, Validation. Zhen-Pei Wang: Writing – review & editing, Conceptualization, Methodology, Software. Yongzhen Mi: Writing, Conceptualization, Methodology, Software. David W. Rosen: Writing – review & editing, Methodology, Supervision. Yingjun Wang: Writing – review & editing, Methodology, Supervision.

Funding This research is supported by the RIE2025 Manufacturing, Trade And Connectivity (MTC) Programmatic Fund < M24N3b0028 > administered by A*STAR and D.W. Rosen's A*STAR start-up fund.

Data availability Data for replication of results will be made available on request.

Declarations

Conflict of interest The authors declare that they have no known competing financial interests or personal relationships that could have appeared to influence the work reported in this paper.

Replication of results Numerical results presented in this study can be reproduced using the algorithm proposed herein. Additional information is available upon reasonable request.

References

Behrou R, Lotfi R, Carstensen JV, Ferrari F, Guest JK (2021) Revisiting element removal for density-based structural topology optimization with reintroduction by Heaviside projection. Comput Methods Appl Mech Eng 380:113799

Bendsøe MD, Sigmund O (2003) Topology Optimization: Theory, Method and Applications. Springer, Berlin

Bluhm GL, Sigmund O, Poulios K (2021) Internal contact modeling for finite strain topology optimization. Comput Mech 67(4):1099–1114

Bodaghi M, Wang L, Zhang F, Liu Y, Leng J, Xing R, Dickey MD, Vanaei S, Elahinia M, Hoa SV, Zhang D, Winands K, Gries T, Zaman S, Soleimanzadeh H, Barši Palmić T, Slavič J, Tadesse Y, Ji Q, Zhao C, Feng L, Ahmed K, Islam Shiblee MDN, Zeenat L, Pati F, Ionov L, Chinnakorn A, Nuansing W, Sousa AM, Henriques J, Piedade AP, Blasco E, Li H, Jian B, Ge Q, Demoly F, Qi HJ, AndréJ-C NM, Fu Y-F, Rolfe B, Tao Y, Wang G, Zolfagharian A (2024) 4D printing roadmap. Smart Mater Struct 33(11):113501

Bruns TE, Tortorelli DA (2001) Topology optimization of non-linear elastic structures and compliant mechanisms. Comput Methods Appl Mech Eng 190(26):3443–3459

Bruns TE, Tortorelli DA (2003) An element removal and reintroduction strategy for the topology optimization of structures and compliant mechanisms. Int J Numer Methods Eng 57(10):1413–1430

Buhl T, Pedersen CBW, Sigmund O (2000) Stiffness design of geometrically nonlinear structures using topology optimization. Struct Multidiscip Optim 19(2):93–104

Cai S, Zhang W, Li Y (2013) Isogeometric shape optimization method with patch removal for holed structures. J Mech Eng 49(13):150–157

Chen Z, Wen G, Wang H, Xue L, Liu J (2022) Multi-resolution nonlinear topology optimization with enhanced computational efficiency and convergence. Acta Mech Sin 38(2):421299

Du B, Zhao Y, Yao W, Wang X, Huo S (2020) Multiresolution isogeometric topology optimisation using moving morphable voids. Comput Model Eng Sci. https://doi.org/10.32604/cmes.2020.08859

Frederiksen AH, Dalklint A, Sigmund O, Poulios K (2025) Improved third medium formulation for 3D topology optimization with contact. Comput Methods Appl Mech Eng 436:117595

Gao J, Xiao M, Zhang Y, Gao L (2020) A comprehensive review of isogeometric topology optimization: methods, applications and prospects. Chin J Mech Eng 33(1):87

Gao J, Wu X, Xiao M, Nguyen VP, Gao L, Rabczuk T (2023) Multipatch isogeometric topology optimization for cellular structures with flexible designs using Nitsche's method. Comput Methods Appl Mech Eng 410:116036

Gomes FAM, Senne TA (2014) An algorithm for the topology optimization of geometrically nonlinear structures. Int J Numer Methods Eng 99(6):391–409

Gupta DK, Langelaar M, van Keulen F (2018) QR-patterns: artefacts in multiresolution topology optimization. Struct Multidiscip Optim 58(4):1335–1350

Han J, Furuta K, Kondoh T, Nishiwaki S, Terada K (2024) Topology optimization of finite strain elastoplastic materials using continuous adjoint method: formulation, implementation, and applications. Comput Methods Appl Mech Eng 429:117181

Han J, Furuta K, Kondoh T, Izui K, Nishiwaki S, Terada K (2025) Topology optimization for nonlocal elastoplasticity at finite strain. Comput Methods Appl Mech Eng 435:117678

Hughes TJR, Cottrell JA, Bazilevs Y (2005) Isogeometric analysis: CAD, finite elements, NURBS, exact geometry and mesh refinement. Comput Methods Appl Mech Eng 194(39):4135–4195

Hughes TJR, Cottrell JA, Bazilevs Y (2009) Isogeometric analysis: toward integration of CAD and FEA. Wiley Publishing

Jahangiry HA, Gholhaki M, Naderpour H, Tavakkoli SM (2022) Isogeometric level set-based topology optimization for geometrically nonlinear plane stress problems. Comput Aided des 151:103358

Keshavarzzadeh V, Kirby RM, Narayan A (2019) Parametric topology optimization with multiresolution finite element models. Int J Numer Methods Eng 119(7):567–589

Klarbring A, Strömberg N (2013) Topology optimization of hyperelastic bodies including non-zero prescribed displacements. Struct Multidiscip Optim 47:37–48

Lahuerta RD, Simões ET, Campello EMB, Pimenta PM, Silva ECN (2013) Towards the stabilization of the low density elements in topology optimization with large deformation. Comput Mech 52(4):779–797

Li J, Ye H, Yuan B, Wei N (2022) Cross-resolution topology optimization for geometrical non-linearity by using deep learning. Struct Multidiscip Optim 65(4):133

Li X, Su H, Yang J, Gao G, Wang Y (2024) NURBS-boundary-based quadtree scaled boundary finite element method study for irregular design domain. Eng Anal Boundary Elem 159:418–433

Li X, Su H, Wang Y (2025a) An improved polygon mesh generation and its application in SBFEM using NURBS boundary. Comput Mech 75(1):265–283

Li X, Mi Y, Wang Z-P, Rosen DW, Wang Y (2025b) Barrier regularization for nonlinear isogeometric topology optimization with large mesh distortion. Eng Comput 41:4529–4548

Lieu QX, Lee J (2017a) Multiresolution topology optimization using isogeometric analysis. Int J Numer Methods Eng 112(13):2025–2047

Lieu QX, Lee J (2017b) A multi-resolution approach for multi-material topology optimization based on isogeometric analysis. Comput Methods Appl Mech Eng 323:272–302

Lin D, Gao L, Gao J (2025) The Lagrangian-Eulerian described particle flow topology optimization (PFTO) approach with isogeometric material point method. Comput Methods Appl Mech Eng 440:117892

Liu J, Zhang H, Min Q, Li P, Yang J, Xia Z (2025) Geometrically nonlinear isogeometric topology optimization via extended finite element method. Comput Struct 316:107871

Nguyen TH, Paulino GH, Song J, Le CH (2010) A computational paradigm for multiresolution topology optimization (MTOP). Struct Multidiscip Optim 41(4):525–539

Nguyen TH, Paulino GH, Song J, Le CH (2012) Improving multiresolution topology optimization via multiple discretizations. Int J Numer Methods Eng 92(6):507–530

Ortigosa R, Martínez-Frutos J (2021) Multi-resolution methods for the topology optimization of nonlinear electro-active polymers at large strains. Comput Mech 68(2):271–293

Park J, Zobaer T, Sutradhar A (2021) A Two-Scale multi-resolution topologically optimized multi-material design of 3d printed craniofacial bone implants. Micromachines. https://doi.org/10.3390/mi12020101

Piegl L, Tiller W (1995) The NURBS book. Springer-Verlag

Qian X (2013) Topology optimization in B-spline space. Comput Methods Appl Mech Eng 265:15–35

Scherz L, Kriegesmann B, Pedersen CBW (2024) A condition number-based numerical stabilization method for geometrically nonlinear topology optimization. Int J Numer Methods Eng 125(23):e7574

Schillinger D, Düster A, Rank E (2012) The hp-d-adaptive finite cell method for geometrically nonlinear problems of solid mechanics. Int J Numer Methods Eng 89(9):1171–1202

Seo Y-D, Kim H-J, Youn S-K (2010) Isogeometric topology optimization using trimmed spline surfaces. Comput Methods Appl Mech Eng 199(49):3270–3296

Sigmund O (1994) Materials with prescribed constitutive parameters: An inverse homogenization problem. Int J Solids Struct 31(17):2313–2329
Sigmund O (1997) On the design of compliant mechanisms using topology optimization*. Mech Struct Mach 25(4):493–524
Sigmund O (2007) Morphology-based black and white filters for topology optimization. Struct Multidiscip Optim 33(4):401–424
Tian J, Li M, Han Z, Chen Y, Gu XD, Ge QJ (2022) Conformal topology optimization of multi-material ferromagnetic soft active structures using an extended level set method. Comput Methods Appl Mech Eng 389:114394
Träff EA, Rydahl A, Karlsson S, Sigmund O, Aage N (2023) Simple and efficient GPU accelerated topology optimisation: codes and applications. Comput Methods Appl Mech Eng 410:116043
van Dijk NP, Langelaar M, van Keulen F (2014) Element deformation scaling for robust geometrically nonlinear analyses in topology optimization. Struct Multidiscip Optim 50(4):537–560
Wang F, Lazarov BS, Sigmund O, Jensen JS (2014) Interpolation scheme for fictitious domain techniques and topology optimization of finite strain elastic problems. Comput Methods Appl Mech Eng 276:453–472
Wang ZP, Poh LH, Dirrenberger J, Zhu Y, Forest S (2017) Isogeometric shape optimization of smoothed petal auxetic structures via computational periodic homogenization. Comput Methods Appl Mech Eng 323:250–271
Wang Y, Wang ZP, Xia Z, Poh LH (2018) Structural design optimization using isogeometric analysis: a comprehensive review. CMES-Comp Model Eng 117(3):455
Xu M, Xia L, Wang S, Liu L, Xie X (2019) An isogeometric approach to topology optimization of spatially graded hierarchical structures. Compos Struct 225:111171
Yin J, Li S, Zhang Y, Wang H (2025) An efficient discrete physics-informed neural networks for geometrically nonlinear topology optimization. Comput Methods Appl Mech Eng 442:118043
Zhang X, Gao L, Xiao M, Gao J (2025) T-splines-based panel method for aerodynamic topology optimization of engineering shell structures using isogeometric analysis. Comput Methods Appl Mech Eng 444:118154
Zolfagharian A, Denk M, Bodaghi M, Kouzani AZ, Kaynak A (2020) Topology-optimized 4D printing of a soft actuator. Acta Mech Solida Sin 33(3):418–430

Publisher's Note Springer Nature remains neutral with regard to jurisdictional claims in published maps and institutional affiliations.

Springer Nature or its licensor (e.g. a society or other partner) holds exclusive rights to this article under a publishing agreement with the author(s) or other rightsholder(s); author self-archiving of the accepted manuscript version of this article is solely governed by the terms of such publishing agreement and applicable law.